DISTRIBUTED ACOUSTIC SENSING APPLICATIONS: FROM SURFACE TO BOREHOLE

by

Joseph A. Mjehovich

A thesis submitted to the Faculty and the Board of Trustees of the Colorado School of Mines in partial fulfillment of the requirements for the degree of Master of Science (Geophysics).

Golden, Colorado

Date _____

Signed: _____

Joseph A. Mjehovich

Signed: _____

Dr. Ge Jin
Thesis Advisor

Golden, Colorado

Date _____

Signed: _____

Dr. Paul Sava
Professor and Department Head
Department of Geophysics

ABSTRACT

Distributed acoustic sensing (DAS) is a relatively new technology used in many geophysical applications. Its first notable use for geophysical monitoring includes downhole deployments for vertical seismic profiling and more recently, hydraulic fracture characterization in unconventional wells. Over the last decade, DAS has extended into broader seismic applications including structural imaging, and near-surface surveys for seismic site classification. Critical to these different applications is the availability of cost-effective methods to acquire data in logistically challenging settings. We propose two novel procedures spanning two distinct industries: (1) using the low-frequency band of DAS to diagnose multi-stage hydraulic fractures in upstream oil and gas, and (2) surface-deployed DAS optical-fiber for low-impact seismic hazard geotechnical surveys.

In 2020, 13 horizontal wells were drilled and completed at the DJ-Postle wellsite, including three wells with various fiber installation methods (permanent, wireline, and disposable) to evaluate completion design efficiency. We apply a geomechanical inversion algorithm to constrain fracture widths using low-frequency DAS (LF-DAS) recorded at an offset well to evaluate the degree of stage isolation in an injection well. LF-DAS indicates incomplete stage isolation in three of the four analyzed intervals, which is validated with distributed temperature sensing (DTS) measurements recorded in the injection well. We find high-frequency in-well DAS measurements are affected by proppant induced erosion and near-wellbore fractures, preventing reliable diagnostics. Implications of our results support LF-DAS for providing critical information for in-well diagnostic interpretations to optimize completion efficiency.

We then leverage the versatility and sensitivity to surface-waves of DAS to examine the potential for using untrenched surface deployments. We acquire continuous DAS data for one hour on a rapidly deployed fiber array composed of six parallel linear subsections laid directly on the surface with different fiber-ground contact conditions. We apply ambient interferometry and adopt a simplified spectral-analysis-of-surface waves (SASW) method to determine the average shear-wave velocity of the top 30 m (VS30). Our methodology results in VS30 estimates for each surface subsection that are consistent with collocated 1 m-depth trenched cables. The implications of these findings support DAS as a viable method for non-invasive deployment surface surveys for earthquake hazard assessment.

TABLE OF CONTENTS

ABSTRACT . . . iii

LIST OF FIGURES . . . vi

LIST OF SYMBOLS . . . viii

LIST OF ABBREVIATIONS . . . ix

ACKNOWLEDGMENTS . . . x

CHAPTER 1 INTRODUCTION . . . 1

1.1 Motivations and Background . . . 1

1.2 How Does DAS Work? . . . 3

1.3 Scope and Outline . . . 3

CHAPTER 2 QUANTITATIVE STAGE ISOLATION EVALUATION USING CROSS-WELL STRAIN MEASUREMENTS . . . 5

2.1 Introduction . . . 5

2.2 Field Description and Instrumentation . . . 6

2.3 In-well DTS Fiber-optic Monitoring . . . 8

2.4 In-well DAS Fiber-optic Monitoring . . . 10

2.5 Offset-well Low-frequency DAS Monitoring . . . 11

2.6 Strain Inversion . . . 12

2.7 Results . . . 14

2.7.1 Treatment Stage 17 . . . 14

2.7.2 Treatment Stage 18 . . . 16

2.7.3 Treatment Stage 19 . . . 17

2.7.4 Treatment Stage 20 . . . 19

2.8 Discussion . . . 20

2.9 Conclusions . . . 23

2.10 Acknowledgements . . . 24

CHAPTER 3 RAPID SURFACE-DEPLOYMENT OF A DAS SYSTEM FOR EARTHQUAKE HAZARD ASSESSMENT . . . 25

3.1 Introduction . . . 25

3.2 Field Description and Data Acquisition . . . 26

3.3 Methodology . . . 28

3.3.1 Ambient-noise Interferometry . . . 28

3.3.2 Dispersion Analysis . . . 28

3.3.3 Estimating VS30 . . . 29

3.4 Results . . . 29

3.5 Discussion . . . 33

3.6 Conclusions . . . 36

3.7 Acknowledgments . . . 36

CHAPTER 4 CONCLUSIONS AND FUTURE WORK . . . 37

4.1 Conclusions . . . 37

4.2 Future Work . . . 38

4.2.1 Low-frequency DAS for Diagnosing Multi-stage Hydraulic Fracture Treatments . . . 38

4.2.2 DAS Surface Deployment . . . 39

REFERENCES . . . 40

APPENDIX A CHAPTER 1 SUPPLEMENTAL INFORMATION . . . 44

A.1 Perforation and Plug Depth Location . . . 44

A.2 In-well DAS Acoustic Intensity Attribute . . . 46

A.3 LF-DAS pre-inversion Processing . . . 48

A.4 Field Strain vs Model Prediction . . . 48

APPENDIX B CHAPTER 2 SUPPLEMENTAL INFORMATION . . . 52

B.1 Spatial Coupling Variation Example . . . 52

LIST OF FIGURES

Figure 2.1 Map view of the Denver Basin including the Greater Wattenberg Field (in red) and the approximate location of the DJ-Postle well site (blue star). 7

Figure 2.2 Gunbarrel view of the well configuration: zipper one wells (green) and zipper two wells (white). Fiber installations include permanent (N1B), temporary wireline (C1), and temporary disposable (N3C). 8

Figure 2.3 Dynamic temperature profile acquired by in-well DTS installation during the hydraulic fracturing treatment of stages 17-20 in well N1B. 9

Figure 2.4 In- well DAS profile acquired during the hydraulic fracturing treatment of stages 17-20 in well N1B. 10

Figure 2.5 Processed low-frequency strain data (top) recorded at offset well C1 during the completion of stages 16-20 in treatment well N1B. The slurry rate (bottom) is plotted for all zipper one wells. 12

Figure 2.6 (a) Strain rate waterfall plot, including picked frac hits for stage 16 (black), stage 17 (blue), stage 18 (yellow), and well C3 (magenta). (b) strain change waterfall plot. (c) Calculated strain change waterfall plot using inverted widths. 14

Figure 2.7 Results for stage 17, including: (a) LF-DAS waterfall plot; (b) in-well DAS waterfall plot; (c) inverted fracture widths grouped by stage interval; (d) in-well DTS waterfall plot; (e)-(f) pumping curves. 15

Figure 2.8 Results for stage 18, including: (a) LF-DAS waterfall plot; (b) in-well DAS waterfall plot; (c) inverted fracture widths grouped by stage interval; (d) in-well DTS waterfall plot; (e)-(f) pumping curves. 17

Figure 2.9 Results for stage 19, including: (a) LF-DAS waterfall plot; (b) in-well DAS waterfall plot; (c) inverted fracture widths grouped by stage interval; (d) in-well DTS waterfall plot; (e)-(f) pumping curves. 18

Figure 2.10 Results for stage 20, including: (a) LF-DAS waterfall plot; (b) in-well DAS waterfall plot; (c) inverted fracture widths grouped by stage interval; (d) in-well DTS waterfall plot; (e)-(f) pumping curves. 19

Figure 2.11 (a) Fracture width change recorded at the end of each treatment stage; (b) temperature difference between the start of treatment and end of treatment; (c) total acoustic energy for each treatment stage. 21

Figure 3.1 DAS deployment overview. (a) Map view of Kafadar Commons showing DAS surface and subsurface deployments. Photographs showing the different surface deployments with black lines superimposed on cables, including (b) Cement north, (c) Grass (left) and Grass Pressed (right), and (d) Cement South, Snow, and Snow Pressed (left to right). 27

Figure 3.2 Stacked correlated ambient waveforms for a single virtual source in the time-space domain for surface subsections (a) Cement North, (b) Grass Pressed, (c) Grass, (d) Snow Pressed, (e) Snow, (f) Cement South, and subsurface subsections (g) Subsurface 1, (h) Subsurface 4. Due to the similarity in results, Subsurface 2 and 3 are omitted from the plot. 31

Figure 3.3 Normalized and stacked dispersion spectra for surface subsections (a) Cement North, (b) Grass Pressed, (c) Grass, (d) Snow Pressed, (e) Snow, (f) Cement South, and subsurface subsections (g) Subsurface 1, (h) Subsurface 4. 32

Figure 3.4 Estimated VR36 results for the Cement North surface subsection. (a) shows the stacked normalized dispersion curve. The dashed line indicates λ=36 m for corresponding phase-velocities and frequencies. (b) indicates the spectral amplitudes for frequency values along the dashed line from (a) with the marker indicating the peak λ=36 m amplitude 33

Figure 3.5 Estimated VS30 results for each linear subsection of the surface array (yellow lines) and subsurface array (red lines). The colored circles and reported values represent the VS30 estimates for the entire length of the corresponding subsection of fiber. Lou et. al. (2020) VS30 estimate was calculated using the entire subsurface array. 34

Figure A.1 In-well DAS (top) recorded in well N1B processed at 500-5000 Hz with temporal acoustic intensity summation (bottom) including (a) stage 17, (b) stage 18, (c) stage 19, and (d) stage 20. The black dashed lines mark the estimated perforation locations. . . 45

Figure A.2 RMS amplitude calculated from in-well DAS (500 - 5000 Hz) for stages 17-20. The black dots indicate the perforation measured depth locations. Offset in the y-direction is to differentiate stages. 46

Figure A.3 In-well DAS recorded during treatment stage 20 (top) and associated pumping curve (bottom). The dashed black lines indicate the bridge plug measured depth for each stage. The red dashed line indicates the interval selected to calculate the noise-floor. . . . 47

Figure A.4 LF-DAS data for treatment stage 18 (top) and associated pumping curves (bottom). (a) Pre-processed LF-DAS data and (b) post processing LF-DAS data. 49

Figure A.5 LF-DAS waterfall plots representing the field strain (a and d) and model predicted strain (b and e) for stage 17 and 18. (c) and (f) compare the predicted strain and field strain at a specific time step. 50

Figure A.6 LF-DAS waterfall plots representing the field strain (a and d) and model predicted strain (b and e) for stage 17 and 18. (c) and (f) compare the predicted strain and field strain at a specific time step. 51

Figure B.1 Map view of Kafadar Field. The purple and red lines indicate the location and ascending channel direction of the Snow Pressed and Snow subsections, respectfully. . . . 52

Figure B.2 Ambient waveforms recorded along Snow Pressed subsection showing how coupling varies spatially across Kafadar Field. From west to east: (a) channel 273, (b) channel 287, (c) channel 296, and (d) channel 306. 53

Figure B.3 Ambient waveforms recorded along Snow subsection showing how coupling varies spatially across Kafadar Field. From east to west: (a) channel 334, (b) channel 325, (c) channel 335, and (d) channel 345. 54

LIST OF SYMBOLS

Angular frequency . . . . . ω

Birefringence scaler multiplicative factor . . . . . ξ

Complex conjugate . . . . . *

Cross-coherence . . . . . ρ

Gauge length L

Material refractive index . . . . . n

Optical phase change . . . . . $\triangle\phi$

Phase velocity c

Poissons ratio . . . . . ν

Stabilization term . . . . . ϵ

Strain rate . . . . . $\dot{\epsilon}$

Vector of station offsets . . . . . h

Virtual receiver V

Virtual source . . . . . U

Wavelenght . . . . . λ

LIST OF ABBREVIATIONS

Carbon Capture Utilization and Storage	CCUS
Colorado School of Mines	CSM
Denver Julesberg	DJ
Distributed acoustic sensing	DAS
Distributed fiber-optic sensing	DFOS
Distributed strain sensing	DSS
Distributed temperature sensing	DTS
Low-Frequency Distributed Acoustic Sensing	LF-DAS
Multi-channel analysis of surface waves	MASW
National Earthquake Hazards Reduction Program	NEHRP
Rayleigh wave phase-velocity at a wavelength of 36 m	VR36
Reservoir Characterization Project	RCP
Root Mean Square	RMS
Spectral-analysis-of-surface-waves	SASW
Time-averaged shear-wave velocity of the top 30 m of subsurface	VS30
Total Organic Carbon	TOC

ACKNOWLEDGMENTS

I would like to start by thanking and acknowledging my advisor, Dr. Ge Jin, for his guidance over the last two years, and providing me the opportunity to be apart of this impactful and exciting work. I would also like to show my appreciation to my committee members, Dr. Jeffery Shragge and Dr. Eileen Martin, for providing me feedback and direction on my research.

I would like to acknowledge the faculty, staff, and students of the Reservoir Characterization Project; their continued support and constructive feedback have been invaluable during this process. I would also like to thank the members of the DJ-Postle project for thoughtful discussion, and our sponsors for funding this work.

Finally, I would like to thank my wife, Lauren, for her unwaivering encouragement and support through all of the time sacrificed, missed date-nights, and mini (sometimes major) meltdowns. I truly would not have accomplished this without you.

CHAPTER 1

INTRODUCTION

1.1 Motivations and Background

Distributed acoustic sensing (DAS) is a rapidly evolving technology belonging to a classification of techniques known as distributed fiber-optic sensing (DFOS), including distributed temperature sensing (DTS), and distributed strain sensing (DSS) [2]. Its first notable geophysical use was in the oil and gas industry for downhole monitoring (i.e., vertical seismic profiling, continuous microseismic, time-lapse monitoring) [2][3], and more recently hydraulic fracture characterization in unconventional lateral wells (e.g.,[4][5]). Within the last decade, the use of DAS has extended into broader seismic applications including but not limited to carbon capture utilization and storage (CCUS) (e.g., [6]), earthquake and aftershock monitoring (e.g., [7][8]), ocean bottom surveys (e.g., [9]), and near-surface imaging in dense urban environments (e.g., [10]).

The aforementioned applications vary widely in their deployment methods, acquisition parameters, and purpose for the end-user. However, they are linked by the versatility of DAS, and its enabling capability to deploy ultra-dense seismic networks at a relatively low-cost. The rapid success of DAS in both industry and academia is arguably the continued demonstration of its practical use in the field. To ensure and accelerate the use of DAS among a diverse range of scientists and technicians, it is critical to innovate multi-domain, cost-effective methodologies. Accordingly, this thesis leverages the high spatial-temporal resolution and exceptional broadband capabilities of DAS to develop two novel methodologies spanning two distinct industries: (1) using the low-frequency band of DAS (LF-DAS) to diagnose multi-stage hydraulic fracture treatments, and (2) surface-deployed DAS optical-fiber for low-impact seismic site classification surveys.

Over the last decade, the evolution of hydraulic fracturing completion designs has simultaneously increased fracture density and lateral well length [11]. Rapid expansion of fracturing efficiency has outpaced the ability to monitor and constrain the complexity during completion phases, limiting available information, and ultimately impacting upstream production. DTS and DAS are two mature methods used for monitoring and diagnosing completion activities in upstream oil and gas. The most common practice includes the permanent installation (i.e., cemented to formation behind wellbore casing) of multi-mode and/or single-mode optical fiber to acquire continuous data during the injection of hydraulic fracturing fluid. However, permanent installation is time consuming and logistically challenging, imposing a significant cost to operators and service companies.

It has been demonstrated that the low-frequency band of DAS contain valuable information critical for characterizing hydraulic fractures [4]. Optical fiber installed in an offset well at some distance away from an injection well, record low-frequency strain perturbations in the surrounding formation caused by approaching and intersecting fractures. This application has been primarily limited to qualitative analysis. Recently, a quantitative approach has been developed by Liu et al. (2021a, 2021b), which constrains the fracture width at an offset well through inversion of the recorded strain measurements. This quantitative analysis capability sets the stage to use LF-DAS as a complementary, or stand-alone hydraulic fracturing diagnostic tool for completion efficiency. Furthermore, use of optical fiber in offset wells does not require permanent installation. Recent field studies demonstrate temporarily deployed cables can produce LF-DAS signals with simlar quality as pernanently installed cables [14][15]. Fiber in an offset well is also not exposed to the risk adverse environment of an injection well, reducing the likelihood of damage and associated cost.

In the last half decade, the popularity of DAS has extended beyond the oil and gas industry, and its applications have grown in near-surface geophysical studies (i.e., engineering, infrastructure, earthquake monitoring). The rapid deployment of dense seismic networks has long been a challenge within the greater seismic community. In recent years, leveraged technology has included portable nodes or geophones, snow streamers (i.e., hydrophones acting as an array on glaciers), land streamers, and the 2D/3D autojuggie [2][16]. However, these methods are all limited by their capabilities to be deployed in different environments. Perhaps the most widely used method for seismic acquisitions, geophones, are difficult to deploy on hard surfaces such as hard-rock layers or cement and asphalt. Additionally, source distribution places constraints on the array geometries, further restricting the use of some seismic instruments.

The versatility and high spatial-temporal resolution of DAS provides an economic low-impact alternative to traditional seismic methods. In recent years, the high sensitivity of DAS to surface waves (i.e., Rayleigh) has been leveraged for near-surface surveys (e.g., [17][1]). Common among these configurations is the trenching of the optical fiber (< 1 m) beneath the surface. While this enhances coupling with the formation to increase signal-to-noise ratio, it also increases the cost and logistics of DAS deployments. It restricts acquisitions to locations with previously installed fiber (so called "dark-fiber") and/or where environmental factors are not a concern. The development and application of low-impact surveys using DAS (i.e., on the ground surface) would greatly contribute to the advancement of its use beyond oil and gas, and demonstrate its value in the broader seismic community (i.e., environmental geophysics, geotechnical surveys).

1.2 How Does DAS Work?

DAS repurposes optical fibers used for telecommunication into multi-channel seismic arrays [17]. Instead of transmitting information, DAS relies on the principles of time-domain reflectometry to effectively turn a length of fiber-optic cable into a continuous network of seismic sensors out to tens of kilometers [2]. The DAS instrument is referred to as an interrogator unit that sends laser pulses into a connected fiber-optic cable. Strain and temperature variations are recorded along the fiber by measuring the properties of backscattered light caused by refractive index heterogeneities in the glass fiber core. Specifically, DAS uses Rayleigh scattering to measure dynamic strain every few meters along the axis of the fiber. Slight perturbations caused by seismic waves or other vibrations change the distance between adjacent sections of the fiber with the return signal carrying information of the disturbance.

Unlike traditional sensors that rely on discrete point measurements, DAS is a distributed sensor that measures strain changes across a length of the fiber known as gauge length, typically between 1-40 m. The gauge length acts as a differential operator across the spatial axis of the data to convert the measurements to strain rate equivalent. The spatial axis of the DAS data is reported in so-called "channels", with much finer spacing than gauge length. Effectively, the spatial resolution of DAS is fixed by the gauge length at a sampling frequency of channel spacing.

1.3 Scope and Outline

In Chapter 2 we develop and demonstrate an effective methodology using LF-DAS data recorded at an offset-well to diagnose multi-stage hydraulic fracture treatments in an unconventional lateral well. This novel approach adopts the geomechanical fracture width inversion algorithm presented by Liu et al. (2021a, 2021b). This study was conducted as part of the larger DJ-Postle Integrated Project, which is the Reservoir Characterization Projects (RCP) primary field project for Phase XIX research. The project includes a multi-disciplinary team of geologist, geophysicists, and petroleum engineers to integrate a comprehensive dataset to evaluate completion efficiency and well communication in the Denver Julesburg (DJ) Basin, Colorado. The well-site, located 20 miles north of Denver, is owned and operated by Great Western Petroleum and includes eight parent wells completed in 2018, and 13 children wells drilled and completed in late 2020. The field provides a robust and unique suite of distributed fiber-optic sensing data, including permanently installed in-well DAS and DTS, and LF-DAS data recorded at wireline retrievable fiber and pump down dissolvable fiber offset wells. The proposed diagnostic method has the potential to complement, or even replace, current in-well diagnostic techniques, at a proportion of the cost.

Chapter 3 develops and demonstrates the ability of surface-deployed DAS cable to record high-fidelity surface waves (i.e., Rayleigh) and produce robust results used for seismic hazard site classification. Data

for the study were collected using the Terra 15 interrogator unit from the DFOS laboratory at the Colorado School of Mines. The study area was also located on the Mines campus at Kafadar Field. The proposed method has promising value in the greater seismic community, specifically for those concerned with geotechnical and civil engineering applications. This methodology can be used in dense urban areas, replacing expensive and invasive traditional surveys (i.e., downhole measurements).

Supplemental information for each chapter have been included in the appendix section. Chapters two and three are slightly modified manuscripts that have been submitted to peer-review journals. Accordingly, they are restricted in their scope, word count, and images based on journal requirements. The supplemental information include additional discussion, data, and images the reader may find crucial to understanding the theory, results, and interpretations presented in the following manuscripts. Specifically, Appendix A is included to expand on the data processing and interpretations for the RCP Phase XIX DJ-Postle field study. Ideally it can be used as a guide, in conjunction with the manuscript (Chapter 2), for future application of the LF-DAS inversion procedure. Appendix B includes further discussion and analysis regarding the lateral variations observed in the recorded ambient waveform results presented in Chapter 3.

CHAPTER 2

QUANTITATIVE STAGE ISOLATION EVALUATION USING CROSS-WELL STRAIN MEASUREMENTS

2.1 Introduction

One of the primary objectives during multiple-stage hydraulic fracturing treatments is the efficient allocation of fluid and proppants into perforation clusters to optimize well performance. The plug-and-perforation (plug-and-perf) completion design in horizontal unconventional wells rely on complete isolation between treatment stages to effectively stimulate the surrounding formation. Stage isolation is achieved when fracturing fluid and proppants exit the wellbore only through perforations at the targeted interval depths. When stages are not well isolated, fluid and proppant leak from the targeted treatment interval into one or more preceding intervals.

Incomplete stage isolation is commonly attributed to partially set bridge plugs, plugs set in deformed casing, and incompatible plug specifications (i.e., size, temperature, pressure ratings) [18]. Significant degradation of both the casing and bridge plug due to proppant-induced erosion can also lead to confinement issues [19]. The loss of stage isolation has a significant impact on treatment efficiency, leading to risks associated with uncontrolled fluid and proppant allocation including damage to the casing and near-wellbore region, and understimulated fractures in the targeted interval [5, 18–20]. Because well completion is often the most expensive cost to operators, the improvement of efficient completion design and diagnostic methods is crucial for optimizing delivery and placement of hydraulic fracturing treatments.

Distributed fiber-optic sensing (DFOS) technology has been increasingly used over the last decade as an advanced monitoring system during completion and production of unconventional wells [4, 21–24]. DFOS uses the principles of time-domain reflectometry to effectively turn a length of a fiber-optic cable into a continuous network of seismic sensors [2]. Strain and temperature variations are recorded along the fiber by measuring the properties of different backscattered lights, including Rayleigh scattering (DAS), Brillouin scattering (DSS), and Raman scattering (DTS). DFOS cable can be either installed inside a well or permanently cemented behind casing, exposing the fiber-optic cable to the effects of fluid flow, temperature changes, and mechanical deformations in the surrounding formation [24].

Current DFOS diagnostics use high frequency DAS and DTS measurements acquired inside the injection well (so called "in-well") during hydraulic fracturing treatments to estimate volumetric fluid distribution at cluster and stage levels [22, 24, 25]. However, in-well measurements are logistically challenging and costly, requiring permanent (i.e., cemented to formation) installation in the wellbore.

Additionally, there is still uncertainty surrounding how best to produce quantitative results with in-well DAS, as it generally relies on empirical models and assumes a correlation between acoustic energy and fluid flow. Qualitative interpretation using DTS is relatively simple, however solving transient temperature behavior requires rather complicated thermal forward modeling to produce quantitative results [24, 26].

Alternatively, DAS cable can be deployed in an observation or offset well to acquire low-frequency strain measurements. Low-frequency DAS (LF-DAS) applications have been largely restricted to qualitative and semi-quantitative analysis to characterize far-field fracture geometry (i.e., fracture height, length, and density) [4, 14]. The development of quantitative methods using LF-DAS is crucial to advance its use for hydraulic fracture diagnostics. Recently, Liu et al. (2021a, 2021b) demonstrate the application of a geomechanical-based inversion algorithm to estimate hydraulic fracture widths using low-frequency strain measured at an offset well. Quantitative analysis in the far-field provides the foundation for using LF-DAS to evaluate treatment efficiency and optimize completion parameters. Additionally, offset well deployments do not require permanent installation and are less likely to be damaged during treatment, substantially reducing the economic risk to operators and service companies.

The objective of this work is to build an approach to diagnose hydraulic fracturing treatment stages using LF-DAS data recorded at an offset well. Our methodology includes qualitative in-well DTS and DAS analysis during the hydraulic treatment of four adjacent stages. We then apply the inversion algorithm proposed by Liu et al. (2021a, 2021b) to the LF-DAS data, constraining far-field fracture widths. Strong agreement between in-well DTS and LF-DAS inversion results confirm incomplete isolation in three of the four stages, while in-well DAS is inconclusive. Results demonstrate that low-frequency far-field strain can be used to confidently diagnose hydraulic fracturing treatments.

2.2 Field Description and Instrumentation

The study area is in the highly productive unconventional play located within the Wattenberg field of the Denver Julesburg (DJ) Basin, Colorado (Figure 2.1). The DJ-Postle well-site is owned and operated by Great Western Petroleum and targets four hydrocarbon bearing horizons: The Niobrara A, B, C, and Codell (Figure 2.2). The Niobrara is a late Cretaceous formation consisting of alternating chalk and marl units, with production generally best in the fractured, high TOC chalk beds. The general thickness of the Niobrara formation ranges from 300-400 ft across the Wattenberg field, with individual chalk beds ranging from 20-50 ft [27]. In the Wattenberg, the Codell is characterized as an impermeable, fine-grained marine shelf sandstone ranging from 5-20 ft in thickness [28].

The DJ-Postle pad includes 13 horizontal wells drilled and completed in 2020 (Figure 2.2). All wells are two-mile laterals with varying completion designs (i.e., stage spacing, cluster spacing, proppant volumes).

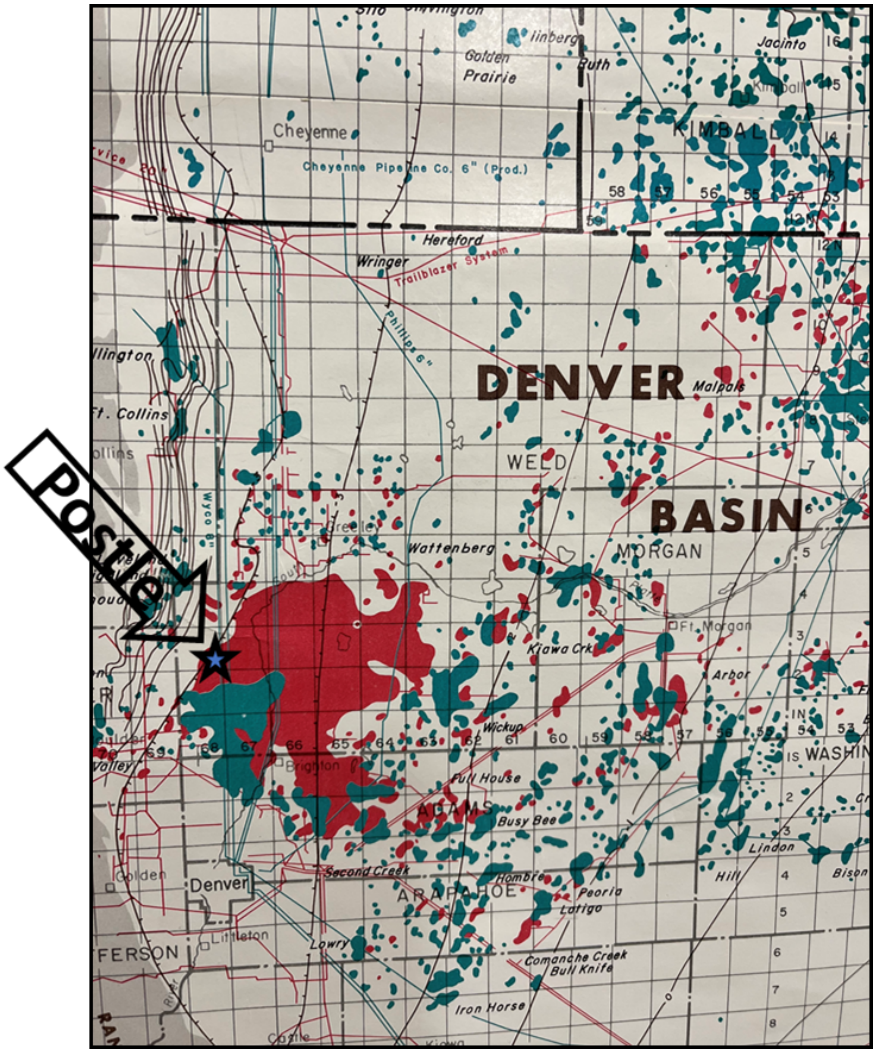

Figure 2.1 Map view of the Denver Basin including the Greater Wattenberg Field (in red) and the approximate location of the DJ-Postle well site (blue star).

The wells were completed by so-called zipper fracking (i.e., hydraulic stimulation of multiple wells in sequence), with two zipper groups operated by two fracking crews, resulting in a complex dataset with up to four different wells being treated simultaneously. This study will focus on zipper group one (green wells in Figure 2.2) which includes seven wells located in the four target formations, completed between November 16^{th} and November 30^{th}, 2020. Each well ranges between 36-51 hydraulic fracture stages resulting in 322 stages total during the two-week period.

Continuous data were acquired by three optical-fiber cables deployed along the length of the wellbores during the two-week operation: (1) a permanently installed (cemented behind the wellbore casing) fiber located in the Niobrara B well N1B highlighted by the magenta pentagon, (2) a retrievable wireline (deployed directly in the wellbore) located in the Codell well C1 highlighted by the green pentagon, and (3)

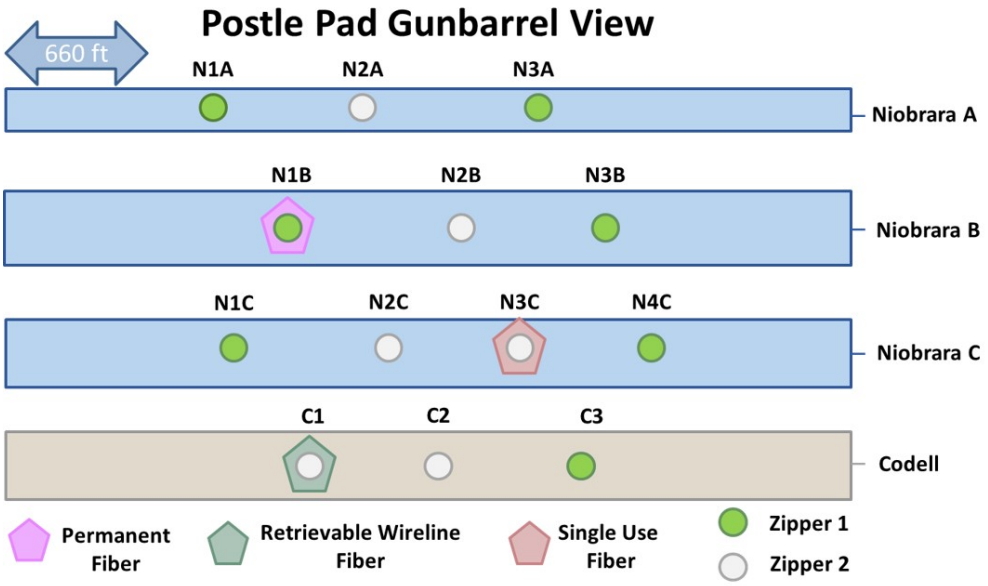

Figure 2.2 Gunbarrel view of the well configuration: zipper one wells (green) and zipper two wells (white). Fiber installations include permanent (N1B), temporary wireline (C1), and temporary disposable (N3C).

a temporary single-use fiber (deployed directly in the wellbore) located in the Codell well C3 highlighted by the pink pentagon. The permanent fiber well N1B was treated during zipper group one, acquiring in-well DAS and DTS data during hydraulic fracturing stages. The temporary wireline fiber well C1 and temporary single-use fiber well N3C monitored the zipper one treatments, acquiring far-field low-frequency distributed acoustic sensing (LF-DAS) signals induced by the nearby injection wells. Additional completion data such as pumping curves (i.e., slurry rate, proppant concentrations, etc.) and high-frequency (10 Hz) pressure gauge data (treatment-pressure) were also acquired.

This study will focus on the subset of stages 17-20 during the treatment of well N1B over the course of approximately 24 hours. Three sets of DFOS data are available for each of the stages: in-well DAS and DTS acquired from N1B in the Niobrara B, and LF-DAS cross-well strain acquired from the temporary fiber well C1 in the Codell. The perforation designs were common to all stages. Cluster spacing was approximately 23 ft, with 12 evenly spaced clusters across 300 ft compartment lengths. Approximately 750 lbs/ft proppant was injected for stages 17-18, and 1000 lbs/ft for stages 19-20, at a maximum rate of 50 bpm.

2.3 In-well DTS Fiber-optic Monitoring

Continuous DTS data were acquired during completion providing the dynamic temperature profile along the Niobrara B N1B wellbore. The DTS profile during the hydraulic fracturing treatment of stages

17-20 are shown in Figure 2.3. Time is along the x-axis and measured depth along the y-axis, increasing from top to bottom (heal to toe). Each stage can be identified in depth and time by the red dashed line, indicating the plug set depth and injection period. The amplitudes in Figure 2.3 indicate the temperature spatially along the fiber over time, with red for the warmest, and dark blue as much cooler.

The cable was installed behind the wellbore casing, allowing for DTS to be recorded during the injection cool-down and post-treatment warm-back period [26]. During hydraulic fracturing treatments, DTS measures the cooling along the entire wellbore caused by the injection of relatively colder fluids and proppants. During a frac-stage, fluid and proppant pass through the heel side causing near uniform cooling. The coolest temperatures are recorded near the stimulated perforation clusters, indicating more direct fluid contact with the optical fiber cable [21, 25]. Post-treatment thermal recovery (warm-back) is observed after injection stops and the near-wellbore region returns to the geothermal surrounding temperature.

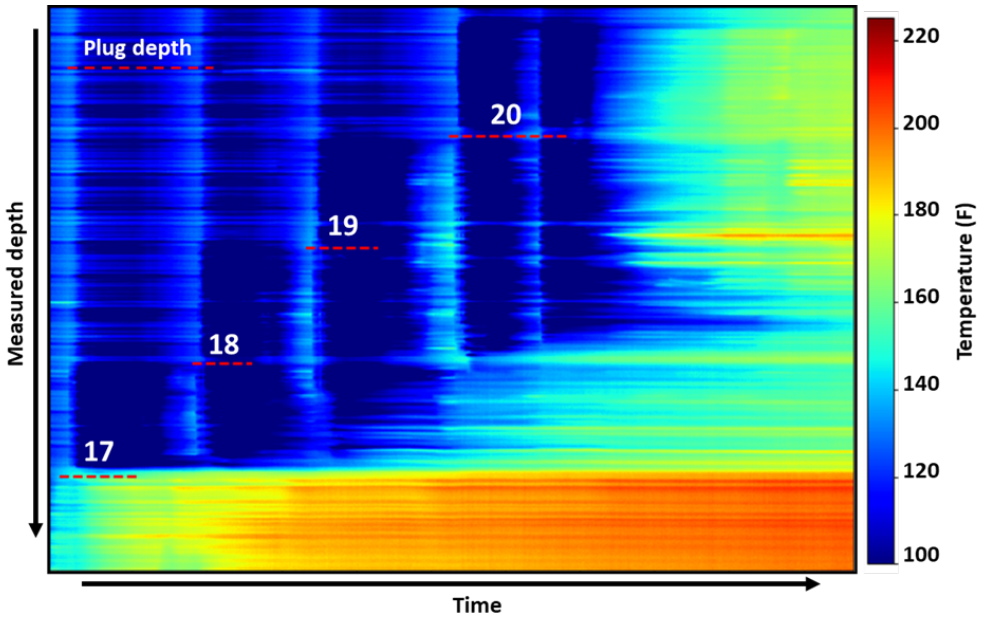

Figure 2.3 Dynamic temperature profile acquired by in-well DTS installation during the hydraulic fracturing treatment of stages 17-20 in well N1B.

We use the indicated bridge plug depths to identify the targeted stage interval. This provides quick, qualitative information describing interstage fluid communication. We then calculate the depth-averaged temperature for each stage during each hydraulic fracturing treatment period. The result is a temperature curve for the current and subsequent treatment stages. The difference between the temperature at the start and end of each treatment period serves as a static, qualitative attribute indicating the fluid intake at each stage interval.

2.4 In-well DAS Fiber-optic Monitoring

Figure 2.4, in which acoustic energy is plotted against time, shows the in-well DAS data acquired during the treatment of stages 17-20. The axes are common with the DTS plot (Figure 2.3), with the plug set depths indicated by the black dashed lines. The red/white in Figure 2.4 represent the high acoustic intensity amplitudes recorded along the DAS fiber at each perforation cluster. The use of in-well DAS for hydraulic treatment diagnosis relies on the correlation of fluid flow rate through perforation clusters and acoustic signatures [21, 24].

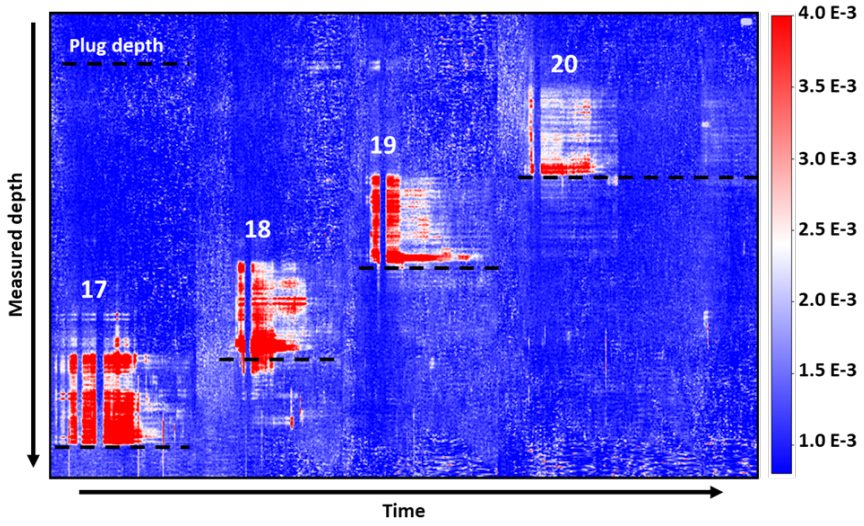

Figure 2.4 In- well DAS profile acquired during the hydraulic fracturing treatment of stages 17-20 in well N1B.

Processing DAS data into different frequency bands is common practice as it allows for the investigation of different physical concepts in and near the wellbore [18]. We utilize the 500-5000 Hz frequency band processed and delivered by the service provider for stage isolation analysis. At this frequency band, acoustic energy amplitudes are assumed to be dominated by "perforation entry noise" and correlate to perforations taking fluid and proppant during the injection period [18, 21]. We identify the bridge plug depths to determine the targeted treatment interval.

We then calculate the RMS amplitudes spatially along the fiber, summing over the treatment period according to:

$$X_{RMS} = \sqrt{\frac{1}{n}\sum_{i=1}^{N} x_{i,j}^2}, \tag{2.1}$$

where $x_{i,j}$ represents the j^{th} DAS channel at the i^{th} time step, and n represents the total number of time steps. The result is an acoustic energy profile, where the highest amplitudes are assumed to correlate to perforations taking in fluid. We adjust the perforation and bridge plug depths reported from the service company by applying a 10 ft bulk shift to better align the perforations and peak amplitudes (see Appendix A for further details).

The data are windowed spatially and temporally according to stage interval depth and the start and end time of each treatment, respectively. The result is four data subsets during each treatment stage. We then calculate the absolute sum of acoustic energy for the windowed data, providing a static, qualitative attribute describing the measured inter-stage acoustic intensity recorded during hydraulic treatment. Additionally, this process is repeated for an upstream section of fiber unaffected by any hydraulic fracturing. This acts as a "noise-floor" used to decouple the targeted DAS signal and any background noise.

2.5 Offset-well Low-frequency DAS Monitoring

The offset-well strain data, shown in Figure 2.5, were acquired from the wireline optical-fiber deployed in the Codell well C1. The raw data were processed to the low-frequency band (< 0.05 Hz) by the service company using proprietary methods. We remove the instrument induced drifts by estimating the drift value using a portion of the data upstream from any fracture hits. Finally, we apply a 2-D median filter with a 3x5 kernel size to remove any data spikes.

The propagation of a hydraulic fracture induces strain perturbations in the surrounding formation [4]. In Figure 2.5, the red and blue amplitudes represent the extending or compressing of the fiber, respectively. When a hydraulic fracture intersects with the fiber ('frac hit'), the portion of the fiber at the fracture hit location is extended, and the surrounding section is compressed when the fracture opens.

Figure 2.5 shows data acquired over a period of approximately 24 hours, including 25 treatment stages zipper fracked across seven different wells (zipper one). The zipper fracking schedule resulted in a complex dataset with strain signals recorded from overlapping and simultaneous treatments of multiple wells. To determine the origin of each strain signal, the slurry rate for each stage was color coded by treatment well and plotted to aid in the interpretation process. While multiple strain signatures were observed in the data, it was determined that the high-amplitude strain (extending/compressing) signals were from treatment well N1B.

Once it was determined which wells the strain signals originate, we first make quick qualitative interpretations to assess treatment stage isolation. By comparing the approximate measured depth of each strain signal in sequence (black dashed arrows), we determine which stages show indications of good isolation or plug failure. Then quantitative interpretations are made through geomechanical inversion.

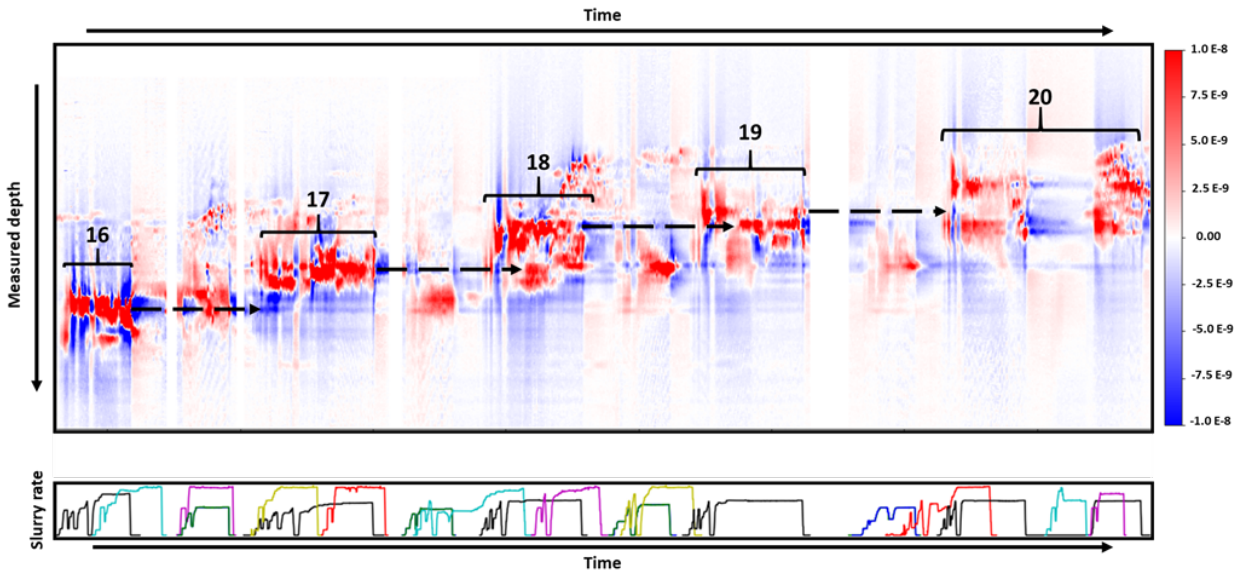

Figure 2.5 Processed low-frequency strain data (top) recorded at offset well C1 during the completion of stages 16-20 in treatment well N1B. The slurry rate (bottom) is plotted for all zipper one wells.

2.6 Strain Inversion

We applied a geomechanical inversion algorithm presented by Liu et al., (2021a, 2021b) to constrain the dynamic fracture widths using LF-DAS data recorded at the offset well C1. While the reader is referred to Liu et al. (2021a, 2021b) for a detailed formulation, the major concepts are summarized below:

- The displacement discontinuity method (DDM) is used to construct a forward model relating LF-DAS strain data to hydraulic fracture geometry. DDM efficiently calculates fracture induced rock deformations in an elastic body.
- The fracture/fiber system is discretized into N fracture elements and M sensing points.
- Assuming linear elastic rock deformation, the strain recorded at a sensing point M, is the superposition of strain contributions from N fracture elements.
- Linear least-squares inversion is used to solve the system of equations for fracture width at discrete timesteps. The LF-DAS data, stored by optical-phase change rate, was converted to strain rate prior to inversion as follows [29]:

$$\dot{\epsilon} = \frac{\lambda}{4\pi n \xi L} \triangle \dot{\phi}, \tag{2.2}$$

where $n = 1.5$ the refractive index, dimensionless; $\xi = 0.8$ a multiplicative constant, dimensionless; $L = 5$ m the gauge length; and $\lambda = 1550$ nm which is the probe wavelength.

Several input parameters must be considered prior to inversion. A parallel orientation between the injector well N1B and monitor well C1 were common in all stages. A 16.4 ft gauge length was used for the LF-DAS. Horizontal and vertical offset were approximately 90 ft and 210 ft, respectively. However, the horizontal and vertical offset values did vary slightly based on the treatment stage. The fracture half-height and half-length were both estimated to be 300 ft. The half-height must be at minimum the vertical distance between wells N1B and C1, likely propagating past C1 given the signal strength observed in LF-DAS Figure 2.5. The fracture half-length was constrained using the horizontal offset (approximately 280 ft) between well N1C and N1B as a proxy. Frac hit signals were observed in LF-DAS Figure 2.5 consistently during the treatment of well N1C. A Poison's ratio of $\nu = 0.29$ was used based on previous work in the nearby Chalk Bluff field as part of RCP's Phase XVIII field project.

We then determined individual fracture hits for treatment stages. Figure 2.6a shows the LF-DAS recorded from monitor well C1 during treatment stage 18 as an example. The dashed lines represent the picked fracture hits as follows: (1) closing fractures from stage 16 (black); (2) reactivated fractures from stage 17 (blue); (3) new fracture hits from stage 18 (yellow); and (4) fracture hits from the Codell well C3 stimulated at the same time (purple). The process for picking fracture hits in a complex dataset rely on:

- The extension zone at the tip of the fractures were frequently observed as a heart-shaped extending pattern at the beginning of the fracture hit signal [4, 14].
- The observed polarity reversal during the step-down, and at the end of fluid injection represent fracture opening (red amplitudes) and closing (blue amplitudes) [4, 14].
- Previous stage fractures are indicated by either: (1) closing signature for the duration of the injection period; or (2) closing signature before injection, and opening signature after injection begins (reactivated fractures).
- Fracture hits and pumping curves were compared temporally to distinguish fracture hits from N1B and C3.

It is worth noting that the fracture hits from well C3 were included during inversion processing, but the results were not considered for this study. This is because (1) there was no in-well data (DAS/DTS) for C3, and (2) the inversion parameters differ from well N1B making the inverted widths unreliable.

The strain rate (Figure 2.6a) was then converted to strain change (Figure 2.6b) by integrating in time. The strain data near the fracture hit locations were removed because decoupling and thermal effects in that region can make the inversion results unreliable [13]. The model predicted strain change (Figure 2.6c) was then calculated using the inverted widths to ensure agreement between the field and modeled data.

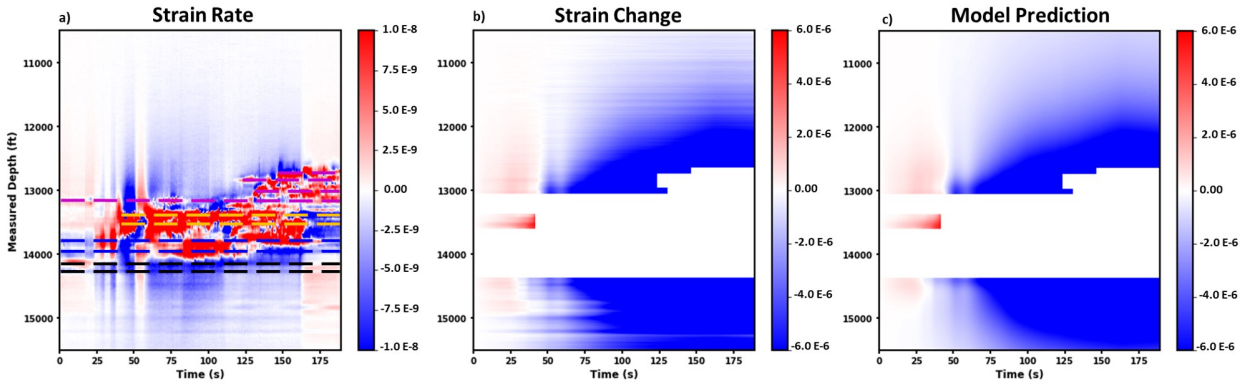

Figure 2.6 (a) Strain rate waterfall plot, including picked frac hits for stage 16 (black), stage 17 (blue), stage 18 (yellow), and well C3 (magenta). (b) strain change waterfall plot. (c) Calculated strain change waterfall plot using inverted widths.

The result is a dynamic width profile for each picked fracture during the injection period. To better diagnose stage isolation, we grouped together fractures common to each stage and summed the widths at each time step. This provides dynamic width profiles at a stage level as opposed to a fracture level. It should be noted that the spatial resolution (5 m) of DAS make it difficult to distinguish if each fracture hit is caused by a single fracture or multiple fractures [4]. In this study, we will assume that each fracture hit is from a single fracture. Because we grouped fractures by stage, the effect on the results is negligible.

2.7 Results

2.7.1 Treatment Stage 17

Figure 2.7 shows the results for stage 17. The top track displays the LF-DAS (Figure 2.7a) and in-well DAS (Figure 2.7b), the middle track displays the width inversion results (Figure 2.7c) and in-well DTS (Figure 2.7d), the bottom track displays the pumping curve information (pressure, slurry, and proppant concentrations) in relative values (Figure 2.7e-f). The in-well DAS, in-well DTS, and LF-DAS plots share the same y-axis (12,000 – 14,500 ft). It should be noted that there is a break in the optical fiber (~14,250 ft) that causes a gap in the DTS data (Figure 6d) and high amplitude noise in the in-well DAS (Figure 6b). All plots share the same x-axis (clock-time). The black and red dashed lines indicate the plug set depth of the current hydraulic fracturing stage.

The DTS profile (Figure 2.7d) indicates good isolation of the current stage from the previous frac stage as no fluid induced cooling (dark-blue) goes beyond the plug set depth. This is further supported by the gradual warming (green to yellow) toe ward from the plug depth. Additionally, the near uniform cooling within the targeted interval indicates that all perforation clusters took in fluid.

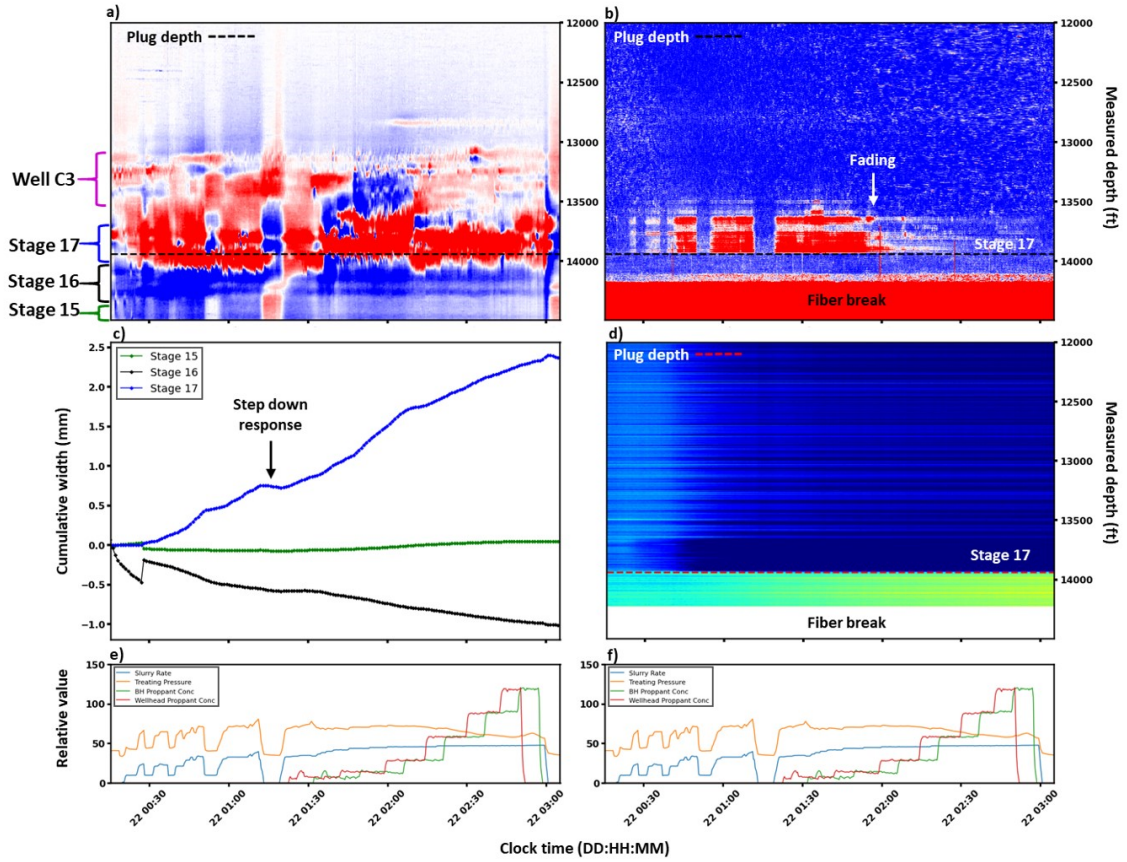

Figure 2.7 Results for stage 17, including: (a) LF-DAS waterfall plot; (b) in-well DAS waterfall plot; (c) inverted fracture widths grouped by stage interval; (d) in-well DTS waterfall plot; (e)-(f) pumping curves.

The acoustic intensity recorded by DAS (Figure 2.7b) during the step-down rate tests and main frac treatment indicate that all 12 clusters took in fluid to some degree. At approximately 1.5 hours the treatment pressure drops coincident with the bottom-hole (BH) proppant concentration increase. Treatment pressure gradually declines while BH proppant concentration incrementally increases for the duration of the treatment. Approximately 2 hours into the injection period, acoustic intensity fades rapidly across all perforation clusters, with only three or four clusters taking most of the fracking fluid by the end of the treatment. Favorable stage isolation is indicated by the lack of acoustic intensity signal below the plug set depth, agreeing with the DTS results.

Newly stimulated fractures within stage 17, and previous fractures from stages 15 and 16 are observed in the LF-DAS (Figure 2.7a). The high amplitude extending strain signal indicates the fractures in stage 17 were opening during the frac treatment. In contrast, the strong compressing signal in stage 16 indicates fracture closure. The extending/compressing strain signals heel ward from stage 17 are determined to be fractures propagating from the treatment of Codell well C3.

The dynamic fracture width profile results are as follows: (1) newly stimulated fractures in stage 17 grow to a sum width of 2.26 mm; (2) fractures from stage 16 close by 1.02 mm; and (3) negligible response is recorded from stage 15 fractures. During the hydraulic fracturing stage, the following observations are noted:

- The inverted fracture width for stage 17 (blue line) indicates strong sensitivity to the in-well injection rate highlighted by the step-down test. The width increase ceases when treatment pressure drops, and increases again when injection resumes.
- Negative width values for stage 16 (black line) indicate fracture closure during the hydraulic fracturing stage (see discussion section).

2.7.2 Treatment Stage 18

Figure 2.8 shows the results for stage 18. Note that the red square along the y-axis of the in-well DAS and DTS (Figure 2.8b and Figure 2.8d) indicate the bridge plug depth of the preceding stage. The in-well DTS profile (Figure 2.8d) shows uniform cooling in the stage 18 interval, suggesting fluid distribution across the stage interval.

The cooling trend toe-ward past the plug depth indicates injection fluid flow into the previously fractured stage. Uniform cooling occurs approximately 20 minutes into the injection period at the stage 18 depth interval while stage 17 cooling occurs gradually toe-ward later into the treatment. Acoustic intensity recorded by DAS (Figure 2.8b) indicate that all 12 clusters took fluid at the start of injection, with most of the fluid flow through the toe-side clusters nearest the plug. Immediately before and after the step-down test, several perforation clusters in the previous stage are reactivated. Approximately 1.5 hours into the injection, there is a sharp decrease in treatment pressure ($\sim$1000 psi) coincident with acoustic intensity fading in stage 18 clusters and an increase in acoustic intensity in previous stage clusters. Acoustic intensity diminishes sharply 2.0 hours into the treatment, and it becomes unclear which clusters were effectively stimulated.

The LF-DAS data (Figure 2.8a) show extending strain at stage 17 and 18 depths and compressing strain at stage 16 depths; indicating opening and closing fractures, respectively. The dynamic width profiles in Figure 2.8c indicate: (1) newly stimulated fractures in stage 18 grow to a width of 2.0 mm; (2) reactivated fractures in stage 17 increase width by 1.2 mm; and (3) fracture widths in stage 16 continuously decreased by 2.1 mm. An inflection in the width profile of stage 17 indicates an increase in the growth rate coincident with the treatment pressure drop. This trend is also observed in the LF-DAS data as a sudden increase in the extending strain at stage 17 depths (Figure 2.8a).

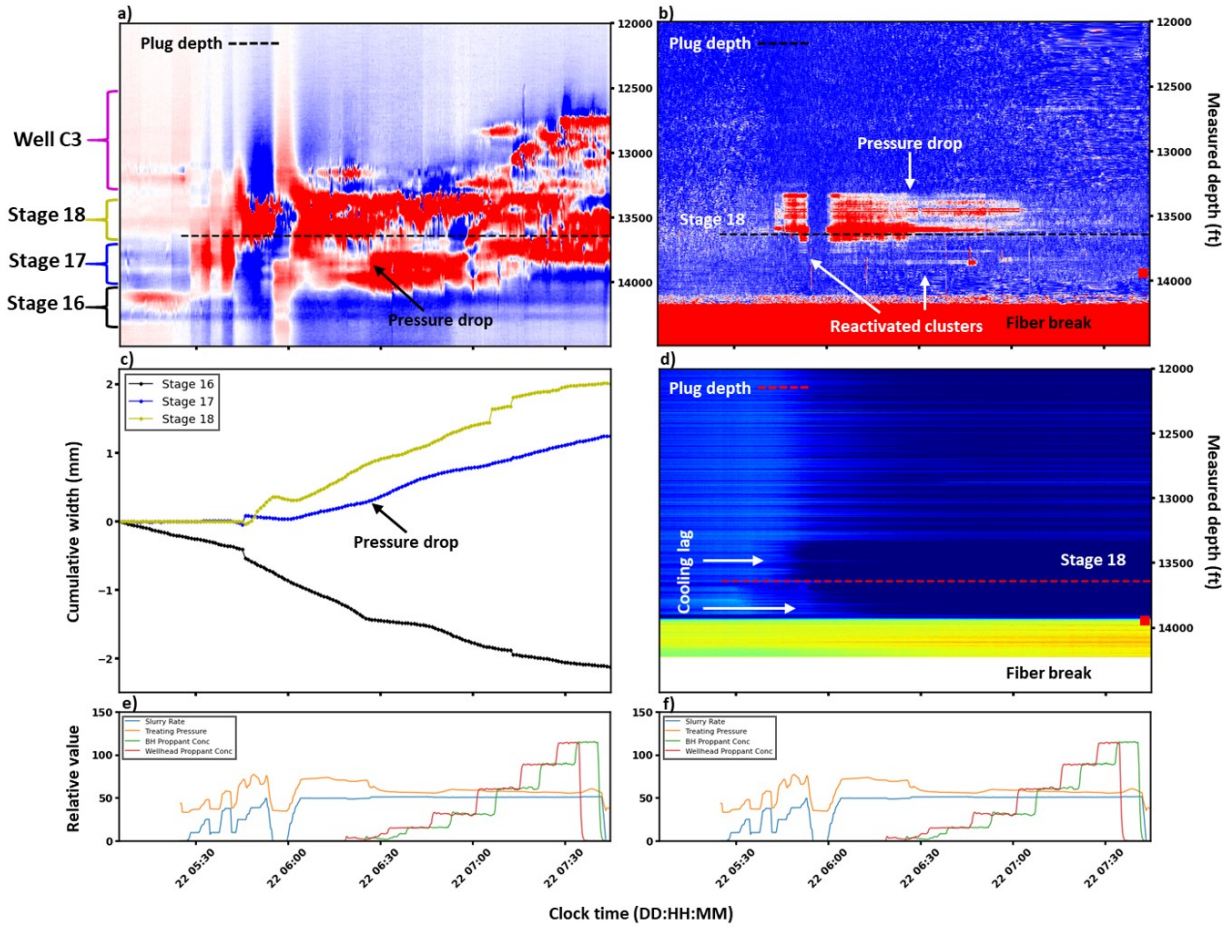

Figure 2.8 Results for stage 18, including: (a) LF-DAS waterfall plot; (b) in-well DAS waterfall plot; (c) inverted fracture widths grouped by stage interval; (d) in-well DTS waterfall plot; (e)-(f) pumping curves.

2.7.3 Treatment Stage 19

Figure 2.9 shows the results during the treatment of stage 19. The in-well DTS profile (Figure 2.9c) shows uniform cooling in the stage 19 interval 30 minutes after injection begins. Fluid continues toe-ward beyond the plug depth into stage 18, uniformly cooling the interval. Fluid also continues into stage 17, where cooling is observed at only half of the interval, suggesting heel-side clusters took more fluid.

Acoustic intensity recorded by DAS (Figure 2.9b) indicate all clusters were stimulated pre and post step-down. After 1.0 hour of injection the acoustic amplitude abruptly diminishes coincident with a sharp drop in treatment pressure (∼1700 psi). Intensity gradually fades during injection, with the heel-side cluster(s) taking most of the fluid as indicated by the high amplitudes near the plug depth. Qualitative observations suggest DAS does not agree with the DTS profile, as there is no indication that perforation clusters were stimulated in the previous stages during injection.

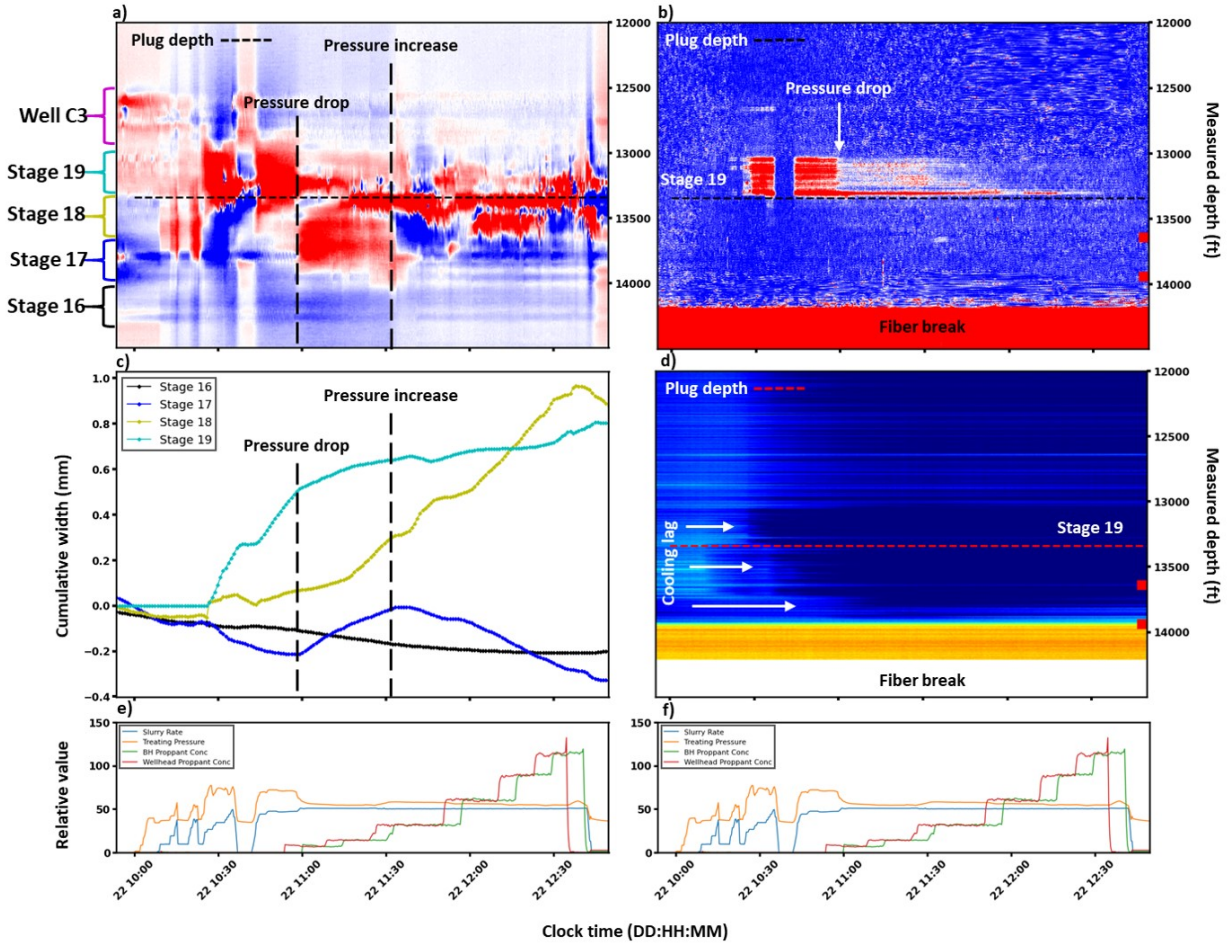

Figure 2.9 Results for stage 19, including: (a) LF-DAS waterfall plot; (b) in-well DAS waterfall plot; (c) inverted fracture widths grouped by stage interval; (d) in-well DTS waterfall plot; (e)-(f) pumping curves.

LF-DAS (Figure 2.9a) indicates new fracture openings in stage 19, reactivated fractures in stages 17 and 18, and fractures closing in stage 16. The dynamic width profile results are as follows: (1) newly stimulated fractures in stage 19 grow to a fracture width of 0.8 mm; (2) reactivated fractures in stage 18 increase width by 0.9 mm; (3) stage 17 fractures decrease width by 0.3 mm; and (4) stage 16 fractures decrease width by 0.2 mm. Several complex fracture interactions are observed in the dynamic width response and LF-DAS during the injection period:

- An inflection point occurs in stages 17-19 coincident with the treatment pressure drop at 1.0 hours into injection. Stage 19 fracture width growth rate decreases while stages 17 and 18 width growth rate increases. Stage 17 notably changes from decreasing width to an increasing width trend.
- Qualitative LF-DAS observations indicate increased extending strain in stages 17 and 18 coincident with the treatment pressure drop.

- A noticeable increase in treatment pressure at 1.5 hours into the injection are coincident with a decreased width growth rate in stage 19, another increase in width growth rate in stage 18, and stage 17 changes from an increasing to decreasing width trend.

2.7.4 Treatment Stage 20

Figure 2.10 shows the results during the injection of stage 20. Note that stage 20 treatment was sectioned into two pumping schedules (20a and 20b). The DTS profile (Figure 2.10d) shows uniform cooling in the stage 20 depth interval. The cooling trend continues toe-ward past the plug depth extending through stage 18. Stage 17 appears to take in fluid at the most heel-ward perforation cluster midway through injection period 20a , with the rest of the stage interval showing a warming trend.

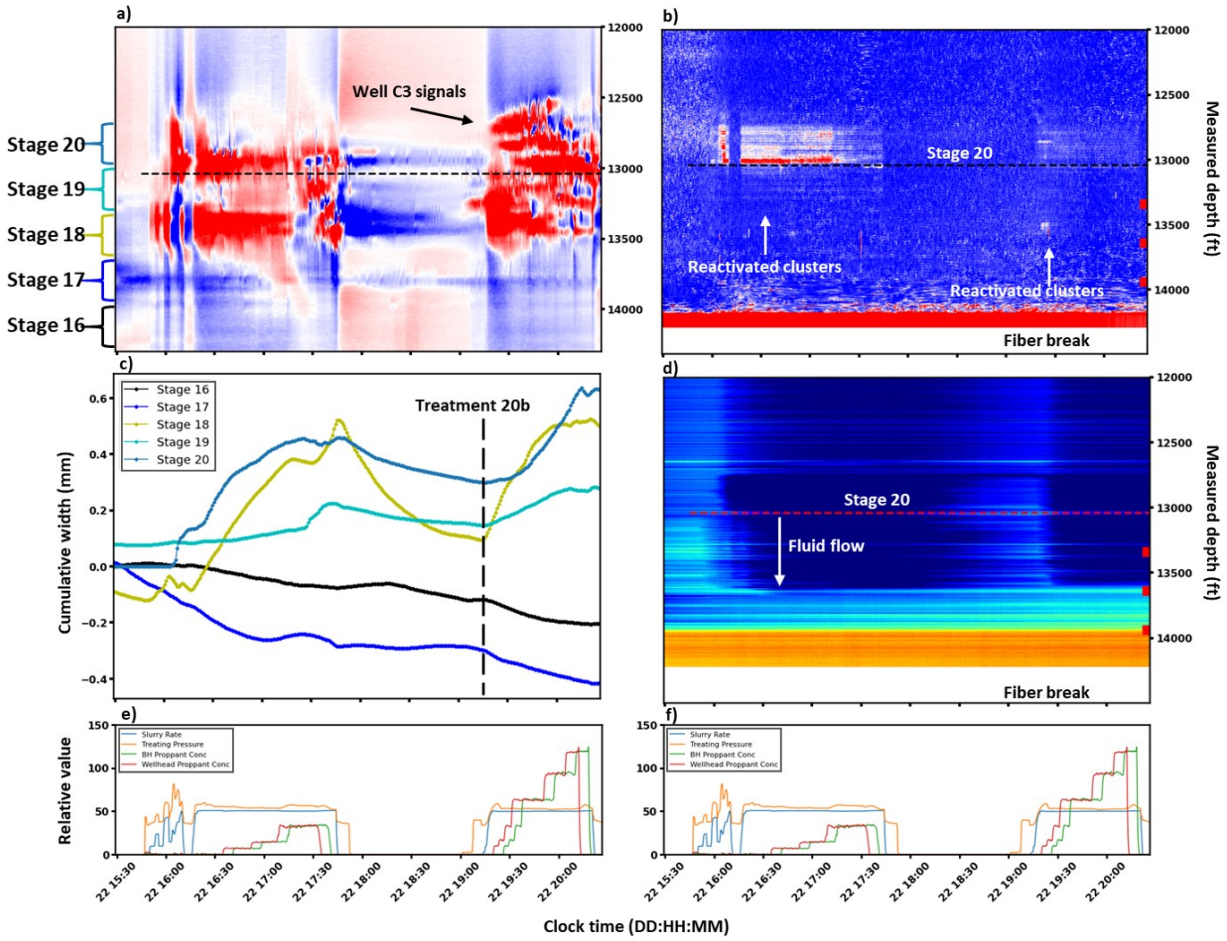

Figure 2.10 Results for stage 20, including: (a) LF-DAS waterfall plot; (b) in-well DAS waterfall plot; (c) inverted fracture widths grouped by stage interval; (d) in-well DTS waterfall plot; (e)-(f) pumping curves.

Acoustic intensity recorded by DAS (Figure 2.10b) indicate all clusters were stimulated pre and post step-down with the toe-ward cluster nearest the plug intaking the most injection fluid. Acoustic intensity

gradually fades uniformly across clusters during injection period 20a and is significantly diminished during injection period 20b . Low amplitude acoustic intensity indicates restimulated perforations in stage 19 interval during treatment period 20a. During treatment 20b, there is an abrupt perf reactivation in stage 18 at clock time 19:30 but diminishes rapidly.

The LF-DAS (Figure 2.10a) indicates newly stimulated fractures in stage 20, and restimulated fractures through stage 17. The dynamic width results are as follows: (1) stage 20 fracture width grows to 0.6 mm; (2) stage 19 fractures are reactivated, growing 0.25 mm, (3) stage 18 fractures are reactivated, growing 0.5 mm; and (4) stage 16 and 17 fractures follow a closing trend, reducing 0.2 and 0.4 mm, respectively. Several observations from the dynamic width profiles worth noting are:

- At 1.5 hours into treatment 20a, stage 17 width changes from decreasing to increasing, which agrees with DTS and LF-DAS profile.
- The beginning of treatment 20b results in the fracture width increasing in stage 18, followed by stage 19, and finally stage 20. This response sequence supports far-field strain as a function of in-well fluid distribution.
- The fracture growth in stages 18-20 increases the closure rate of stage 16 and 17 indicated by the width results following the start of treatment 20b.
- Signals from Codell well C3 are visible in the LF-DAS during treatment 20b.

2.8 Discussion

Extending our analysis across multiple treatment stages permits the integration of in-well and offset-well methods for a comprehensive diagnosis. Our study indicates robust agreement between in-well DTS and LF-DAS inversion results. Figure 2.11a shows the cumulative fracture width changes for each substage, recorded at the end of the targeted treatment stage. Positive and negative column values represent fracture opening and fracture closure, respectively. Similarly, Figure 2.11b represents the spatially averaged temperature difference between the start and end of the targeted treatment stage. Positive column values represent cooling from fluid contact, and negative values represent warming from favorable stage isolation.

DTS and LF-DAS inversion indicates in three of four stages monitored, fluid leaked below the plug, and stage isolation was not complete. During the hydraulic fracturing treatment of stages 18-20, fluid flows into one or more of the previous stage compartments, cooling that section of fiber to near fluid temperatures. Accordingly, the far-field response is constrained by LF-DAS inversion, showing a decrease in stimulated fracture widths across the actual treatment stages. During the treatment of stage 17, isolation is complete, and no fluid flow past the bridge plug is observed. Showing strong agreement, LF-DAS inversion indicates

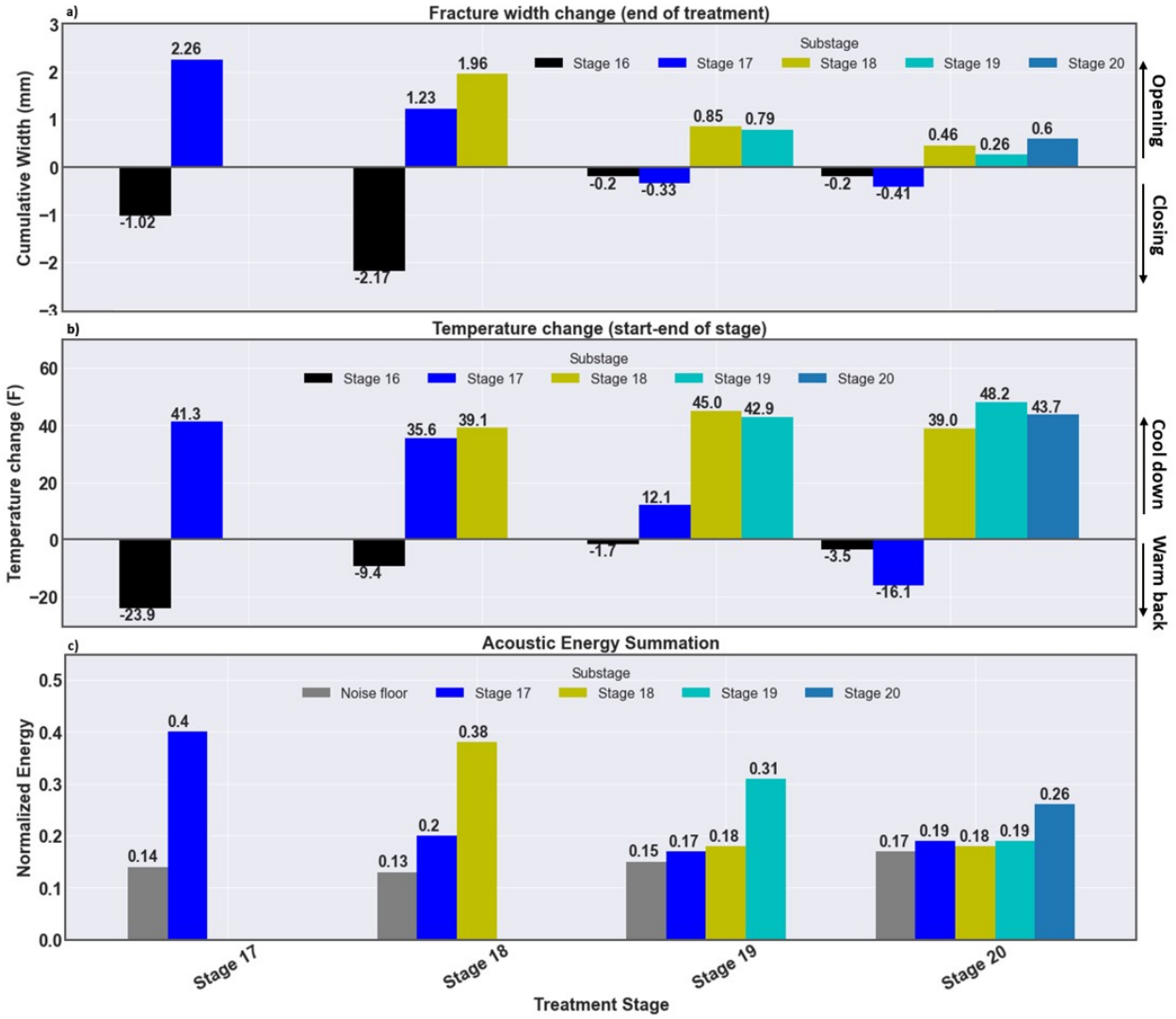

Figure 2.11 (a) Fracture width change recorded at the end of each treatment stage; (b) temperature difference between the start of treatment and end of treatment; (c) total acoustic energy for each treatment stage.

optimal fracture growth in the targeted treatment stage, while stage 16 fracture widths decreased significantly. However, during the treatment of stages 18-20, inter-stage fluid communication extends into adjacent stage intervals, and fracture widths for both the targeted and previous treatment stages diminish. In general, we observe a 73% difference in fracture width growth for the targeted treatment stage between the stages 17-20.

The observed decrease in fracture width is likely due to near-wellbore region (NWR) and far-field effects. In the NWR, inter-stage fluid communication effectively increase the compartment length from 300 ft to 900 ft, affecting cluster efficiency, fluid distribution and proppant placement [30]. In the far-field, opening fractures suppress the nearby rock formation, leading to the closure of nearby fractures [12].

In contrast, assuming a relationship between fluid flow rate and acoustic intensity, in-well DAS shows little evidence of poor stage isolation. Figure 2.11c shows the normalized acoustic energy summation for all current and previous hydraulic fracturing stages, including the calculated noise floor for each. Theoretically, high acoustic intensity at perforations below the stage plug of the targeted interval describe the degree of fluid flow into previous stages [22, 24]. While the acoustic intensity follows the same diminishing trend for the targeted treatment interval ($\sim$35% between stage 17 and 20), there is little indication of cluster restimulation. Interpretations based on in-well DAS alone would suggest that isolation issues occur only during the treatment of stage 18 (Figure 2.11c, Figure 2.8b).

The absence of DAS intensity at restimulated clusters is likely due to variations in the wellbore region. The acoustic intensity fading in our results (Figure 2.7b, Figure 2.8b, Figure 2.9b, Figure 2.10b) is commonly observed when proppant reaches the perforation clusters [26]. Proppant induced erosions occurs, beveling and smoothing the edges of the perforation holes, reducing the amount of friction and noise despite treating pressure remaining relatively constant [26, 31]. Accordingly, the acoustic intensity generated by reactivated clusters is very weak and can hardly be differentiated from the background noise recorded by DAS.

The sensitivity of the LF-DAS inversion to in-well variations is highlighted by stages 18 and 19 (Figure 2.8 and Figure 2.9). Midway through hydraulic treatment, a significant pressure drop is observed in the pumping curves coincident with an inflection point in the LF-DAS inversion results. Specifically, we see previous stage fracture widths grow at a faster rate than the targeted treatment stage. The response is also observed in LF-DAS (Figure 2.8a and Figure 2.9a) as an abrupt extension signal. This indicates that the pressure drop occurs due to inter-stage fluid communication, the effects of which are observed in the far-field and quantitatively constrained by restimulated fracture widths. Important to note is that the in-well DAS (Figure 2.8b and Figure 2.9b) show a significant drop in acoustic intensity at the targeted clusters but no noticeable change below the bridge plug depths. This could be misleading, suggesting that

the pressure drop is due to an increase in BH proppant concentraions and/or proppant induced erosion of the perforation holes.

The implications of our findings demonstrate LF-DAS recorded in an offset well is a viable method for multi-stage hydraulic fracturing treatment diagnosis. LF-DAS inversion can be used to constrain far-field fracture widths to evaluate completion efficiency and design optimization. In-well variations (i.e., inter-stage fluid communication, bridge plug failure) can be identified and quantitatively described in the far-field through fracture width inversion. Volumetric estimates can be made by placing additional constraints on restimulated fractures (i.e., fracture shape) to determine the fluid distribution between current and previous stage fractures.

Installation of permanent in-well optical-fiber is expensive and requires careful consideration of placement along the wellbore to avoid damage during hydraulic fracturing [18]. Temporary wireline deployments in an offset well are considerably less expensive and require less considerations during installation (i.e., cementation to formation, configuration). In operations where in-well DAS is deemed too costly or there is adverse risk, temporary fiber installations can be used to monitor hydraulic fracture treatments.

2.9 Conclusions

We demonstrate the effectiveness of using DAS installed in an offset well to diagnose multi-stage hydraulic fracturing treatments. We apply a geomechanical based inversion algorithm to the low-frequency strain data to quantitatively describe the time evolution of fracture widths in the far-field. We use the inverted fracture widths to diagnose stage isolation and bridge plug failure and verify our results using in-well DTS and DAS. Our major findings include:

- In-well DTS and cross-well LF-DAS inversion show strong agreement regarding plug integrity evaluation, indicating poor stage isolation and/or bridge plug failure in three of four investigated treatment stages.
- Poor stage isolation results in significantly decreased fracture widths recorded at the monitor well in the current treatment stage. This is due to decreased in-well cluster efficiency, and far-field stress shadowing.
- In-well DAS fails to diagnose inter-stage fluid communication in all but one of the treatment stages. The absence of reactivated perforation noise is likely due to proppant induced erosion effects during treatment.

- A significant pressure decrease in the wellbore during injection is observed as an increase in fracture width in previous stage intervals, and the suppression of fracture width increase in the targeted treatment stage.

2.10 Acknowledgements

We would like to thank Great Western Petroleum for providing the data and guidance for this study. We would also like to thank the sponsors of the Reservoir Characterization Project (RCP) at the Colorado School of Mines for enabling this research to be conducted. Special thanks to Travis Payeur and Rick Gibson from NanoSeis (now Halliburton) for their support with data processing and guidance. This chapter was converted from a manuscript first-authored by Joseph Mjehovich, and co-authored by Dr. Ge Jin, and Dr. Kan Wu. My contributions in the work include developing workflows used for data processing prior to inversion, the application of the inversion algorithm, and analysis and interpretation.

CHAPTER 3

RAPID SURFACE-DEPLOYMENT OF A DAS SYSTEM FOR EARTHQUAKE HAZARD ASSESSMENT

3.1 Introduction

Variations in near-surface soft soil deposits are thought to largely dictate seismic amplitudes on a local scale [2, 32, 33]. The time-averaged shear-wave velocity of the top 30 m (VS30) has been the quantitative parameter adopted by NEHRP (National Earthquake Hazards Reduction Program) for site classification and building codes in the United States for nearly two decades [34–36]. Site class is used to characterize soil properties and determine the local seismic coefficients for earthquake-resistant structural design [35, 37]. For large-scale commercial buildings and city infrastructure, the difference between site classifications can substantially affect the initial and long-term cost of construction [37]. VS30 has also been widely used as a parameter for characterizing effects of soil stiffness on ground-motion prediction studies [38–40].

Traditional VS30 surveys generally are invasive, use logistically challenging borehole measurements (i.e., crosshole, suspension logging methods), and require prior authorization to implement [35, 36, 41]. Accordingly, current VS30 maps are spatially limited in coverage. In areas where no VS30 data are available, estimates often rely on interpolated values or broadband and long-period permanent seismic arrays that suffer from reliability and resolution due to poor station distribution [2]. The development of non-invasive techniques that measure surface wave dispersion properties address many of the challenges associated with VS30 surveys and greatly improve data coverage and availability for structural engineers. Within the last two decades, the spectral-analysis-of-surface-waves (SASW) method has been widely used for cost-effective, non-invasive site classification studies [37, 41–43].

In recent years, distributed acoustic sensing (DAS) has emerged as a reliable tool for near-surface applications and subsurface characterization. Its versatility and high spatial-temporal resolution make it a suitable instrument for non-invasive VS30 surveys. DAS uses the principles of time-domain reflectometry to effectively turn a length of a fiber-optic cable into a linear network of seismic sensors out to tens of kilometers [2]. Dynamic strain is recorded along the fiber by measuring the phase difference of backscattered light caused by impurities in the fiber core. DAS is mostly sensitive to particle motion along the axis of the fiber, making it highly effective for measuring the horizontal component of surface waves (i.e., Rayleigh). Recent applications use pre-existing unused telecommunication networks (i.e., so-called "dark fiber") to record high-quality seismic data from earthquakes [7–9] as well as ambient and anthropogenic sources in dense urban areas [44–46]. In locations where dark fiber is unavailable, traditional

deployment methods consisting of burying (< 1 m) DAS cables [1, 17] are used to ensure sufficient coupling and higher signal-to-noise ratios. However, this approach often proves cost prohibitive and logistically challenging to implement.

Research concerning the instrument response of DAS cables deployed directly on the ground surface is sparse. Spikes et al. 2019 demonstrate that helically wrapped cables draped along the ground surface recorded similar quality active-source (i.e., hammer shots) reflection data as collocated geophones. High-fidelity data acquisition from surface DAS arrays could provide geotechnical engineers with an efficient and cost-effective method for numerous near-surface applications. In this study, we compare ambient waveform data recorded by a surface-deployed DAS array with those recorded from collocated trenched cables. We adopt a simplified SASW method to estimate VS30 for linear subsections of both arrays.

The paper begins with a description of the unique deployment of the DAS arrays and the data acquisition parameters used for the field study. We then discuss our data processing approach, which includes ambient-data interferometry, dispersion curve mapping, and generating VS30 estimates. This is followed by a presentation and discussion of our results for each data processing step. We find that further analysis of the ambient waveforms and dispersion curves provides important qualitative information such as signal coherency and dispersion features to compare the different coupling conditions. A quantitative comparison of our VS30 results shows that using surface-deployed DAS cables is a viable approach for near-surface geotechnical surveys. We conclude with potential implications for the application of surface DAS fiber deployments.

3.2 Field Description and Data Acquisition

The field test was conducted at Kafadar Commons located on the Colorado School of Mines campus. Kafadar Commons is a rectangular grass field approximately 40 m by 100 m in size. At the time of data acquisition, the southern half of the field was covered by several inches of snow while the northern side was exposed grass.

We deployed 650 m of optical fiber along the surface of the field and connected it to the 1-km trenched DAS array previously installed beneath Kafadar Commons as part of the Mines Underground Geophysical Laboratory (see Figure 3.1) [47]. The surface array was deployed as six parallel lines roughly 100 m in length using two different coupling methods: (1) laid directly on the ground; and (2) pressed into the ground by several people walking on top of the cable. Cables deployed under condition (2) will be referred to as 'Pressed'. The first line segment was draped along the cement walking path north of the field (Cement North), followed by two lines along the grass (Grass Pressed and Grass), and two lines along the snow (Snow and Snow Pressed). The final line segment was deployed along the cement walking path south

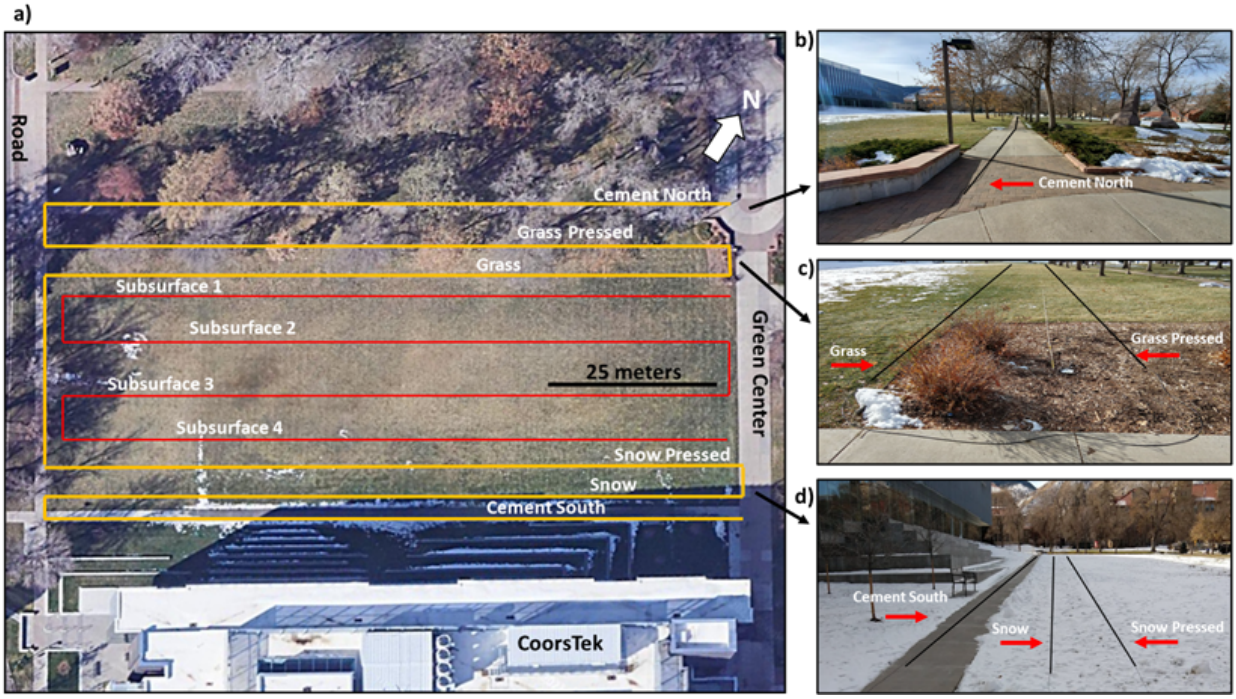

Figure 3.1 DAS deployment overview. (a) Map view of Kafadar Commons showing DAS surface and subsurface deployments. Photographs showing the different surface deployments with black lines superimposed on cables, including (b) Cement north, (c) Grass (left) and Grass Pressed (right), and (d) Cement South, Snow, and Snow Pressed (left to right).

of the field (Cement South) and terminates inside the adjacent CoorsTek building (see Figure 3.1a). Parallel line segments were separated by approximately 2.5 m, except the Cement North (Figure 3.1b) and Grass Pressed (Figure 3.1c) segments which were separated by approximately 7.5 m, and the Grass (Figure 3.1c) and Snow Pressed segments by 30 m (Figure 3.1d). The overall footprint of the surface array is 45 m by 100 m.

The trenched array follows a 27 m by 90 m grid pattern located 1 m beneath the surface (Luo et al., 2020). To examine nearly coincident instrument responses, we only use data recorded along the four subsections (Subsurface 1-4) running parallel to the surface array. The two subarrays were connected by splicing the end of the surface cable to the fiber-optic lead of the subsurface cable located in the CoorsTek building. We calibrated the DAS channel locations using GPS coordinates, tap-tests, and hammer-shot data.

The range of detectable wavelengths is constrained by the receiver (DAS channel) spacing Δx_{min} and the array aperture Δx_{max} along the linear subsections of the array. Wavelengths shorter than twice the channel spacing of the array will be spatially aliased according to the Nyquist theorem. In general, the longest resolvable wavelengths are twice the array aperture. For the frequency-phase velocity relationship,

the aliasing and resolution boundaries can be expressed as $2f * \Delta x_{min}$ and $2f * \Delta x_{max}$ ([1]).

Approximately 1.0 hour of data were recorded on December 2nd, 2020, using a Terra15 Treble interrogator unit at a 4467 Hz sampling rate with a channel spacing of approximately 2.45 m. A gauge length of 4.0 times the channel spacing was used, which acts as a differential operator across the spatial axis of the data to convert the measurements to strain rate equivalent. We recorded ambient waveforms from anthropogenic sources in the survey area, including a nearby road running orthogonal to our array setup approximately 5 m from the nearest DAS channel.

3.3 Methodology

3.3.1 Ambient-noise Interferometry

We use ambient seismic interferometry [48, 49] to produce virtual shot gathers for each linear profile of the surface and subsurface arrays. With this approach, each DAS channel along a linear segment of fiber is considered a virtual seismic source (U_i) or receiver (V_i). We partition the 1-hr record of data into 2.0-s time windows and then calculate and stack the cross-spectrum [50] according to

$$\rho(x_s, x_r, \omega) = \sum_{i=1}^{N} \frac{U_i(x_s, \omega) V_i^{\star}(x_r, \omega)}{|U_i(x_s, \omega)||V_i(x_r, \omega)| + \epsilon} \tag{3.1}$$

where ω is angular frequency, U_i and V_i are the Fourier transform of the ith time segment of two virtual stations, and x_s and x_r are the spatial locations of the virtual source and receivers, respectively. * denotes the complex conjugate, and real positive constant ϵ is a stabilization term. Individual cross-spectra are calculated for all possible station pairs, resulting in 7162 virtual shot-receiver pairs. The 2.0-s windows are stacked in the frequency domain, with the resulting cross-spectrum returned to the time domain by applying an inverse Fourier transform. The resulting waveform has positive and negative time-lags representing waves propagating in opposite directions between the virtual stations [49]. Applying this method within each linear subsection and treating each DAS channel as a virtual source produces corresponding 3-D waveform volumes that are analyzed for data quality prior to dispersion analysis.

3.3.2 Dispersion Analysis

To produce frequency-velocity dispersion images we use the phase-shift method [48]. With this method, we can separate the different surface-wave modes despite the relatively limited number of traces and offsets from our virtual shot gathers. The first step is to extract the wavefield phase by applying a temporal Fourier transform to the virtual shot gathers (ρ) produced in equation 3.1. Next, we apply the offset-dependent phase shift and normalize the amplitudes to ensure equal weighting for each individual

trace:

$$P(\omega, c) = \sum_{x_s} \sum_{h} \frac{\rho(x_s, h, \omega)}{|\rho(x_s, h, \omega)|} \mathrm{e}^{-\mathrm{i}\omega \mathrm{h}/\mathrm{c}}, \tag{3.2}$$

where $h = x_s - x_r$ represents a vector of station offsets. The maximum amplitude term occurs when signals travel at the same phase velocity (c) for a given angular frequency. This produces a frequency-velocity dispersion image for each channel serving as a virtual source along each linear profile. Because the primary goal is to produce VS30 estimates for each linear subsection, we stack the dispersion images of all virtual sources from the same linear profile to produce a single dispersion image for each subsection.

3.3.3 Estimating VS30

We estimate VS30 for each subsection using a simplified SASW method [34]. Compared to the traditional SASW approach, this method is computationally efficient but provides only a single VS30 value without using traditional inversion methods that produce 1D shear-wave velocity profiles for a range of depths. The correlation between Rayleigh-wave phase velocity and VS30 can be described by the predictive empirical equation [34]:

$$VS30 = 1.076 \times VR36, \tag{3.3}$$

where VR36 is the Rayleigh wave phase-velocity at a wavelength λ=36 m. Extracting VR36 from the processed dispersion curves results in a phase velocity and amplitude for discrete frequencies within the chosen frequency band. Frequency resolution is determined by two parameters: (1) the raw data sampling rate and as consequence of the Fourier transform, and (2) the window length of the processed ambient time series. A cubic interpolation method was applied to each dispersion image to improve the frequency resolution prior to VS30 processing. We determine the final VS30 value for each subsection using the VR36 value with the highest amplitude in the dispersion image.

3.4 Results

Figure 3.2 displays the examples of ambient waveforms for surface array subsections (a)-(f) and two subsurface array subsections (g)-(h) after transforming the cross-spectra to the time-space domain. Offsets for each subsection vary slightly due to differences in cable length. The observed waveform direction reversal is due to subsections being deployed in an east-west or west-east orientation. The high-amplitude zero offsets of the waveforms represent the source channel autocorrelation of each virtual shot gather. After applying a 2-20 Hz bandpass filter and manually scanning for data quality, we find most virtual shot gathers exhibit coherent waveforms. Figure 3.2 highlights offsets with poor signal response. Notably, the Snow subsection lacks coherent waveform features along 40 m of the fiber and, to a lesser extent, the Grass

Pressed and Snow Pressed subsections display poor data quality along 12 m of fiber. The waveforms for all subsections display an asymmetric distribution, which is discussed in detail below.

Figure 3.3 shows the stacked, normalized dispersion curve results for the surface (a)-(f) and subsurface (g)-(h) profiles for the 3-20 Hz frequency band and a 100-2000 m/s phase velocity range. The most stable results are within the lower frequency range of 3-7 Hz defined by the high spectral amplitudes in red. All dispersion curves show an abrupt discontinuity between 7-9 Hz, potentially indicating a mode transition [1]. Coherency in the dispersion curves begins to diminish at higher frequencies, with no continuous dispersion features above 20 Hz. The subsurface subsections show the most consistent results with relatively well-defined spectral amplitudes for frequencies below 15 Hz. These are followed by the Cement North, Grass, and Grass Pressed subsections that show stable results for frequencies less than 12.5 Hz. The Snow Pressed subsection is stable for frequencies less than 11 Hz, and finally the Snow and Cement South subsections are stable for frequencies below 10 Hz.

The Rayleigh wave phase velocity primarily depends on the subsurface geomechanical properties (i.e., shear-wave velocity, and to a lesser extent, compression-wave velocity, and density) down to a depth of one wavelength, with maximum sensitivity at approximately $\frac{1}{2}$ to $\frac{1}{3}$ the wavelength ([34]). Accordingly, shorter wavelengths describe the shallower subsurface, with longer wavelengths providing material properties at greater depths. The frequency-phase velocity maps (Figure 3.3(a)-(f)) for the surface subsections provide reliable estimates between wavelengths of approximately 40 m and 125 m (4 Hz - 10 Hz). In some sections, frequencies beyond 10 Hz become less reliable due to the lack of coherent dispersion features. The subsurface sections (Figure 3.3(g)-(h)) demonstrate coherent dispersion features up to 15 Hz corresponding to a wavelength of approximately 20 m. The maximum wavelength that can be recovered from seismic interferometry is limited to the array size, due to the interference between forward and backward propagating wavefields. In this study, however, we are able to make reliable measurements to the wavelengths longer than the linear sections. One potential reason is that because the noise sources are biased to one-side of the array, the effect of interference is minimized.

VR36 values were estimated using the dispersion curves for each subsection. Figure 3.4 shows the results for the Cement North profile as an example. The dashed line in Figure 3.4a represents the phase-velocity and frequency values corresponding to a wavelength of 36 m (VR36). Figure 3.4b tracks the normalized spectral amplitude as a function of phase velocity for discrete frequencies along the VR36 line. The marker denotes the peak amplitude which is the value used to calculate VS30 for each subsection (Figure 3.5). Note that Grass Pressed and Cement South returned peak spectral values along the VR36 line corresponding to a phase velocity of 279 m/s and 705 m/s, respectively. Prior to calculating the VS30 value for these subsections, we analyzed their dispersion curves and found that the second highest spectral

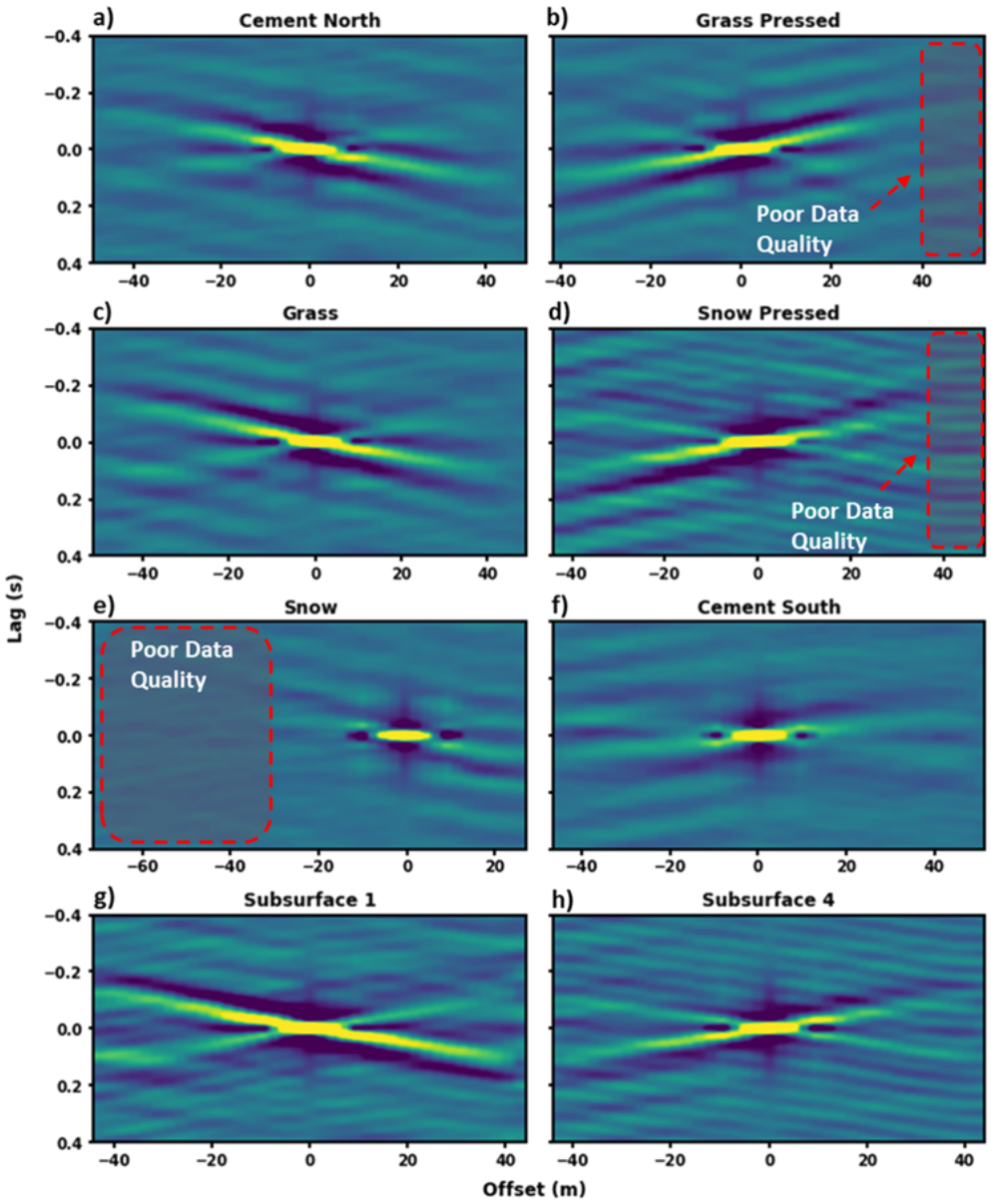

Figure 3.2 Stacked correlated ambient waveforms for a single virtual source in the time-space domain for surface subsections (a) Cement North, (b) Grass Pressed, (c) Grass, (d) Snow Pressed, (e) Snow, (f) Cement South, and subsurface subsections (g) Subsurface 1, (h) Subsurface 4. Due to the similarity in results, Subsurface 2 and 3 are omitted from the plot.

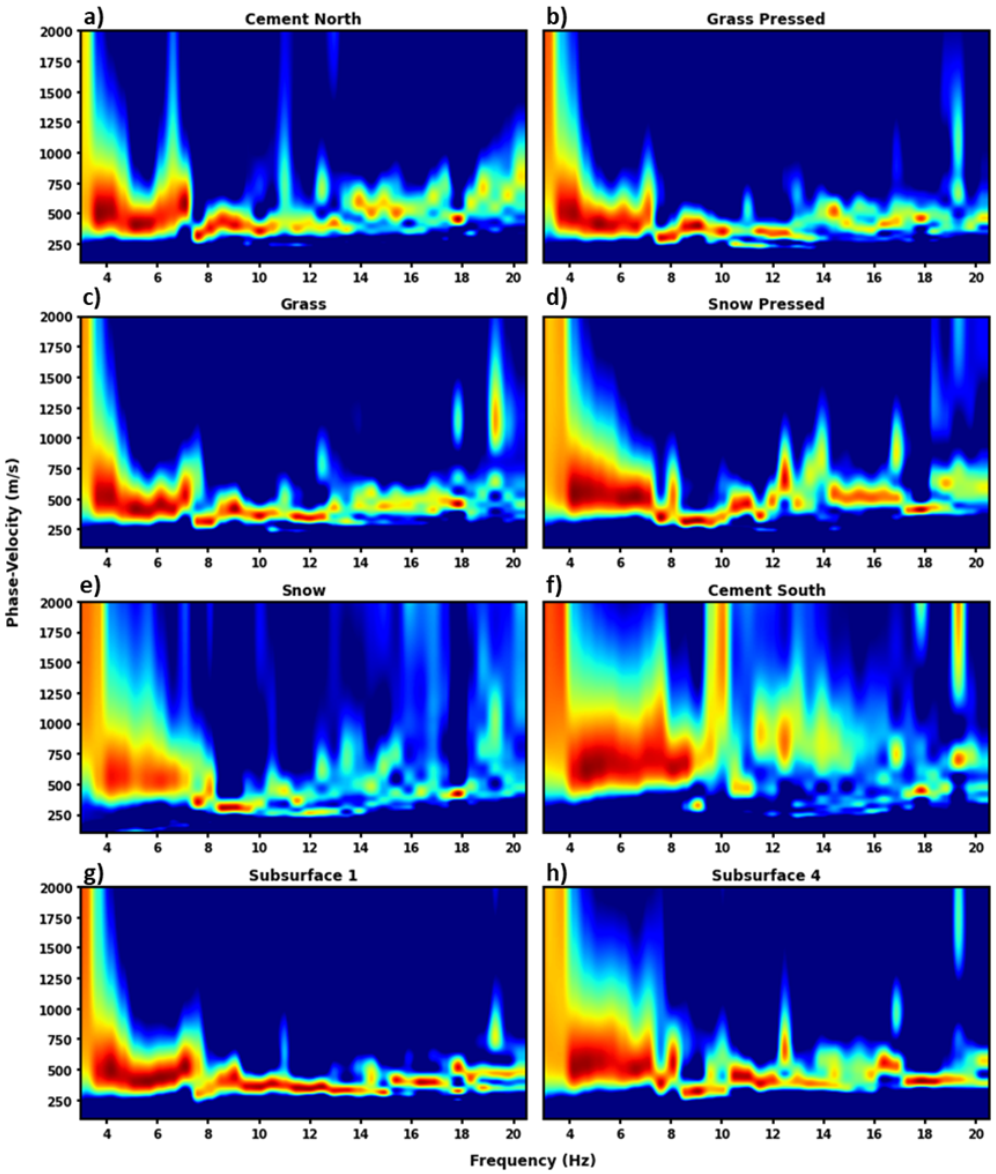

Figure 3.3 Normalized and stacked dispersion spectra for surface subsections (a) Cement North, (b) Grass Pressed, (c) Grass, (d) Snow Pressed, (e) Snow, (f) Cement South, and subsurface subsections (g) Subsurface 1, (h) Subsurface 4.

values compared well to the phase velocities of adjacent subsections, which are plotted in Figure 3.5

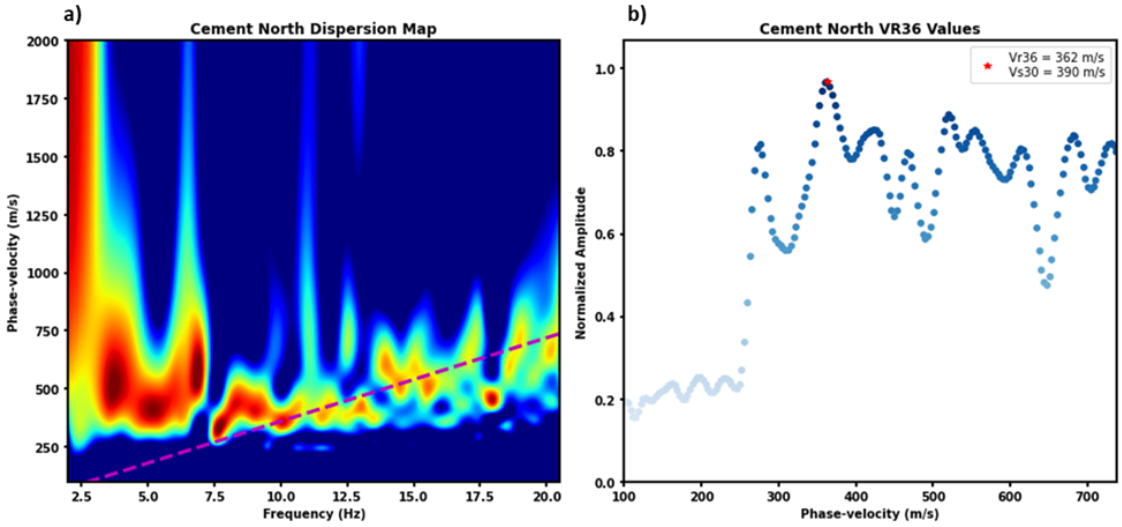

Figure 3.4 Estimated VR36 results for the Cement North surface subsection. (a) shows the stacked normalized dispersion curve. The dashed line indicates λ=36 m for corresponding phase-velocities and frequencies. (b) indicates the spectral amplitudes for frequency values along the dashed line from (a) with the marker indicating the peak λ=36 m amplitude

We compare our results to a previous study that uses more sophisticated methods to analyze ambient data acquired from only the subsurface array. Luo et al. (2020) present a detailed 1-D S-wave velocity profile using a multimodal Monte Carlo inversion method for the first 120 m of the subsurface. We find that their numerical results suggest a VS30 estimate of approximately 370 m/s for the entire survey area. This result falls within approximately 5% of our VS30 estimates along the north side of the field, and 9% toward the south side (Figure 3.5).

3.5 Discussion

Figure 3.2 shows that the time-domain waveforms for all subsections exhibit asymmetric behavior. The observed effect is an amplitude difference between signals traveling along the positive (causal) and negative (acausal) time lags. Ideally, these signals would be identical if the sources of ambient energy were distributed homogeneously throughout the survey area [49]. However, the waveform asymmetry is likely due to the heavy traffic on the road directly to the west (Figure 3.1). We make this interpretation based on: (1) the road running perpendicular to the DAS subsections; and (2) the proximity (approximately 5 m) to the nearest DAS channel. The DAS instrument response is highly sensitive to propagating waves with particle motion oriented along the fiber axis. Thus, the primary source of energy is likely from the high-amplitude surface waves generated by nearby traffic noise.

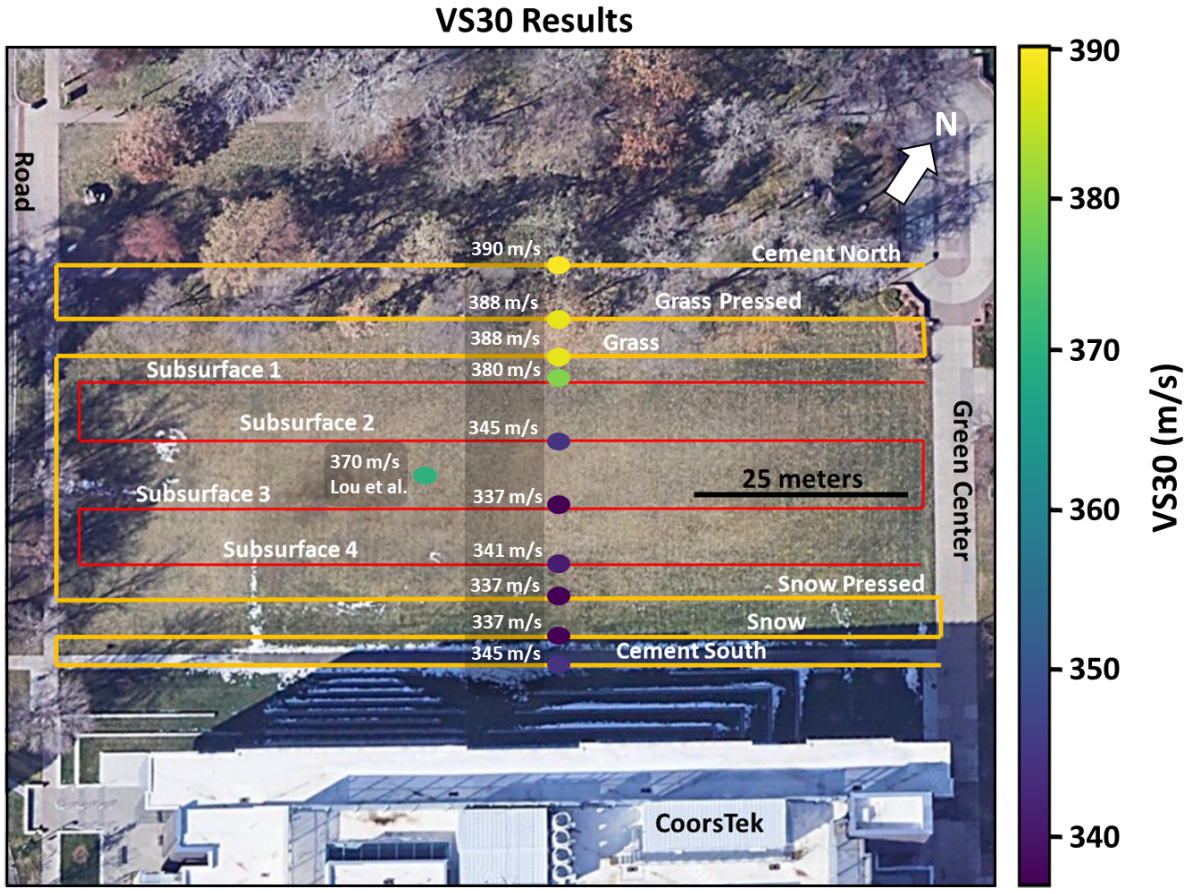

Figure 3.5 Estimated VS30 results for each linear subsection of the surface array (yellow lines) and subsurface array (red lines). The colored circles and reported values represent the VS30 estimates for the entire length of the corresponding subsection of fiber. Lou et. al. (2020) VS30 estimate was calculated using the entire subsurface array.

The spectral differences presented in our results commonly arise when applying an interferometric approach to field data [49]. The asymmetry in ambient waveforms is a consequence of wavefield energy distribution and array geometry. The most effective seismic array geometries for near-surface surveys require consideration of the spatial distribution of ambient energy sources. Dominant noise sources (e.g., roads) should be of particular importance [17]. This is especially true in terms of time and cost if sensors were trenched prior to data acquisition. The novelty of our surface deployment minimizes the economic risk involved in both static and time-lapse surveys, allowing for flexible installations and rapid reconfiguration of seismic arrays if necessary.

Our study indicates that robust VS30 estimates can be made from linear DAS arrays deployed directly on the ground surface. Further analysis of the ambient waveforms and dispersion curves provides qualitative information describing the coupling of each subsection. In general, we observe that waveform

coherency, high-amplitude moveouts, and continuous dispersion curves result from superior coupling conditions. Clear examples are the substantial difference in signal response for the Snow and Snow Pressed subsections. The response along the Snow returns a relatively low-amplitude coherent waveform with moveout at -30 m to 30 m offsets (60 m) along the fiber, whereas the Snow Pressed subsection results in a higher amplitude, coherent waveform with moveout across most of the fiber (90 m). We also see more continuous dispersion features for the Snow Pressed subsection in comparison to the Snow subsection (Figure 3.3). This suggests that simply pressing the fiber into the snow by walking on it improves the fiber-ground contact and significantly enhances the energy transfer and signal response (see Appendix B for further discussion).

Figure 3.5 shows the VS30 trend with a decreasing velocity from the northern to the southern halves of the field defined by a discontinuity between Subsections 1 and 2. While a full geologic interpretation goes beyond the scope of this study, a straightforward explanation for the decreasing velocity trend would be lateral subsurface variations. It is possible this observation is due to differential soil compaction in the field, with less consolidated soil to the south of Subsection 1 due to the Mines Underground Geophysical Laboratory installation [47]. The primary takeaway from our study is the consistent VS30 estimates for collocated subsections of the surface and subsurface arrays given the different coupling conditions.

Practical applications of our findings include several near-surface geophysical surveys. Site classification for earthquake hazard assessment can use our approach in areas where there is insufficient VS30 coverage, and traditional seismic analysis methods are impractical and costly (i.e., urban areas). DAS surface deployments can be easily implemented by a small team in a timeframe of hours as opposed to days compared to traditional trenched techniques, and do not require gaining access to subsurface conduits or trenching. Additionally, our methodology and the flexibility of DAS offers geotechnicians the spatial resolution to constrain lateral variations in the velocity structure throughout a survey site as seen in our results.

Rapid deployment of dense seismic networks is crucial for acquiring critical data immediately following mainshock earthquakes [8]. Current DAS aftershock monitoring deployments use pre-existing teleseismic networks ("dark fiber"), which are restrictive in availability and spatial distribution [7, 8]. Shear-wave velocity characterization using permanently installed strong motions stations also suffer the same limitations [51, 52]. The ability to rapidly deploy DAS cables along the surface addresses these issues as a standalone network or to provide complementary data along with traditional methods. Furthermore, surface-wave methods often rely on sophisticated inversion techniques to estimate subsurface structures. The simplified SASW approach adopted in our study is an easily automated workflow and can be used by research and industry technicians to reduce computational expense for rapid VS30 estimations.

3.6 Conclusions

We demonstrate the effectiveness of DAS to record dynamic strain from surface waves generated by anthropogenic activity when deployed directly on the ground surface under different coupling conditions. We deployed a DAS array composed of six parallel linear subsections along the ground surface above preinstalled collocated trenched cables buried 1 m below. Applying an interferometric approach to 1.0 hour of recorded data, we show that the resultant waveforms and dispersion curves contain qualitative information describing the variable coupling of each linear subsection. Coherent high-amplitude waveforms, moveouts across channels, and continuous dispersion features characterize the coupling quality. Furthermore, ambient waveform asymmetry suggests that the data are influenced by the spatial distribution of dominant energy sources, highlighting the importance of flexible seismic array installations. By adopting a simplified spectral-analysis-of-surface-waves (SASW) method that does not require inversion, we produce robust VS30 estimates consistent for collocated subsections despite the differences in coupling condition. Implications of this study suggest that DAS can be rapidly deployed along the ground surface to acquire high-quality data for a variety of near-surface seismic applications.

3.7 Acknowledgments

The instrumentation used for this study belongs to the DFOS laboratory at Colorado School of Mines. . We would like to thank Dr. Richard Krahenbuhl and Dr. Whitney Trainor-Guitton for facilitating the fiber installment of the Mines Underground Laboratory. We would also like to acknowledge Dr. Bin Luo for his research involving the Mines Underground Laboratory fiber installment which has been cited in this study. This chapter was converted from a manuscript first-authored by Joseph Mjehovich, and co-authored by Dr. Ge Jin, Dr. Eileen R. Martin, and Dr. Jeffery Shragge. My contributions in the work include assisting in the deployment, acquisition, and data processing. I developed the workflows and codes used for this study including cross coherence and dispersion processing and analysis.

CHAPTER 4
CONCLUSIONS AND FUTURE WORK

In the preceding chapters we demonstrate the versatility and multi-domain capabilities of DAS through the practical application of two distinct and novel methodologies. This work spans two very different industries and audiences: (1) exploration (i.e., oil and gas), and (2) geotechnical. Critical to both is the availability of cost-effective methods to acquire robust data in logistically challenging settings. We leverage the exceptional broadband frequency response of DAS, and its high spatial-temporal resolution to address these challenges. Our developed methodology are computationally efficient, simple to automate and integrate into existing workflows, and offer an economic alternative to established methods. Although our results are promising and validate the multi-functional use of DAS in conjunction with our proposed methodology, we acknowledge the potential for further development. Therefore, we offer several areas of future work to be considered.

4.1 Conclusions

Chapter 2 demonstrates that DAS can be deployed in an offset well to diagnose multi-stage hydraulic fracturing treatments in the far-field. We apply a geomechanical inversion algorithm to quantitatively constrain fracture widths using low-frequency DAS data which can be interpreted to evaluate the degree of inter-stage fluid communication in an injection well (i.e., poor stage isolation, bridge plug failure, casing failure). The unique optical-fiber deployment at the DJ-Postle well site provides the opportunity to compare offset well LF-DAS interpretations with established in-well diagnostic methods (i.e. DAS and DTS). LF-DAS results indicate incomplete stage isolation in three of four analyzed intervals, which is validated with in-well DTS analysis. However, in-well DAS interpretations suggest only one of four stages suffers from poor stage isolation. We conclude that the in-well DAS measurements for the targeted treatment stages are unreliable due to in-well and near wellbore region erosion effects (i.e., proppant induced erosion of perforation holes and, near-wellbore fractures).

Perhaps the most significant result is the sensitivity of the inversion algorithm to variations in the injection well. Notably, we observe abrupt pressure changes in the injection well coincident with fracture width changes in the offset well at least 250 ft away. Integrating our analysis across all four targeted stages shows the effects of poor stage isolation on completion efficiency. As inter-stage fluid communication propagates into adjacent stages, fracture width growth diminishes substantially in the far-field.

The implications of our results promote the use of LF-DAS to acquire a suite of diagnostic information. Qualitatively, it can be used to identify inter-well communication in the far-field, constraining fracture height, length, density, and azimuth. Quantitative constraints can be placed on fracture width simultaneously providing critical information for in-well diagnostic interpretations to optimize completion parameters. LF-DAS installations in an offset well can substantially lower the risk associated with costly and challenging in-well installations for operators and service companies. Finally, our developed method is computationally efficient and can be automated to handle large scale completion operations.

Chapter 3 demonstrates the viability of DAS to record high-fidelity surface waves deployed directly on ground surfaces under different conditions. We collected 1.0 hr of ambient data on a surface deployed DAS array and verified our results with the collocated trenched array 1 m beneath the surface. We applied a simplified multi-channel analysis of surface waves which includes ambient interferometry resulting in estimated VS30 across Kafadar Field located on the Colorado School of Mines campus. We find that VS30 estimates result in an approximate 15% spatial variability across the width of the field (45 m).

This field study highlights the exceptional sensitivity of DAS to record surface waves, which is critical for MASW surveys. Despite relatively light coupling conditions, each section of fiber recorded sufficient signal response to produce consistent VS30 estimates with only 1.0 hr of data. The cross-coherence and stacking process associated with ambient interferometry successfully offset the poor signal to noise ratio synonymous with poor coupling conditions, resulting in coherent waveforms and dispersion spectra.

The developed method has practical application for the greater seismic community (i.e., earthquake aftershock monitoring, regional scale imaging). However, geotechnicians would likely benefit the most, as our method could possibly be implemented into existing MASW workflows used for site classification surveys. An additional benefit is that DAS surface deployments are low impact, and do not require negotiation of challenging installations (i.e., burying the cable, downhole measurements). Finally, the use of DAS among the geotechnical community would significantly impact exposure and commercialization, further advancing a rapidly developing technology.

4.2 Future Work

4.2.1 Low-frequency DAS for Diagnosing Multi-stage Hydraulic Fracture Treatments

Quantitative analysis using in-well measurements to estimate fluid flow volumes would be the next logical step in the development of this method. DAS and DTS fluid flow modeling could be used to verify our results beyond qualitative analysis. Placing constraints on the fracture geometry recorded at an offset well would enable far-field fluid volume estimates to be compared with in-well modeling, possibly establishing a relationship between the two. Ideally, fractures measured at multiple offset wells could be

used to reduce the amount of unknown parameters and uncertainty associated with the fluid volume measurements.

Further automation of the workflow would permit large-scale diagnostics for hydraulic fracturing treatments. Qualitative analysis (i.e., fracture length, height, azimuth) coupled with quantitative (i.e., fracture width) constraints could provide unprecedented information critical to optimizing completion design and well spacing. The availability of this data for an entire well completion would provide the information needed to make geomechanic interpretations complementary to current methods used for reservoir characterization.

4.2.2 DAS Surface Deployment

During our analysis we found that the the Grass Pressed and Cement South subsections returned peak spectral values resulting in VS30 estimates far outside the range of the other subsections. After further analysis, we found that the second highest peak spectral value resulted in VS30 values consistent with the other subsections. We postulate that this is likely due to the relatively sparse frequency resolution from our dispersion processing. Although we applied interpolation to enhance the resolution, perhaps a finer or more advanced interpolation should be applied to address this issue. The quality of the Cement South subsection was relatively poor, thus interpreting the second highest spectral peak can be argued. However, the dispersion curve for the Grass Pressed was much higher quality, leading to uncertainty in our interpretations. This is an important issue to address because if this method was applied in the field, the deployment configuration may not have multiple subsections to aid with interpretations.

There is a notable difference between the dispersion curves observed for Cement South and Cement North, with the former lacking any coherent dispersion features above 9 Hz. The deployment of both subsections was identical outside of the location in the study area. It is possible that the observed effect is caused by noise from the nearby CoorsTek building. Cement South is the subsection closest to the building, and is also the tail end of the array which was deployed inside CoorsTek where it was connected to the subsurface array.

Calculating V_s models using more sophisticated inversion methods on each subsection and comparing with V_s models from the subsurface array would be the next step to verify our results. V_s model comparison using traditional methods (i.e., geophone deployment) would likely resonate with the general seismic community on a greater scale.

REFERENCES

[1] B. Luo, W. Trainor-Guitton, E. Bozdağ, L. LaFlame, S. Cole, and M. Karrenbach. Horizontally orthogonal distributed acoustic sensing array for earthquake- and ambient-noise-based multichannel analysis of surface waves. *Geophysical Journal International*, 222(3):2147–2161, 2020.

[2] Z. Zhan. Distributed Acoustic Sensing Turns Fiber-Optic Cables into Sensitive Seismic Antennas. *Seismological Research Letters*, 91(01):1–15, 2020.

[3] B. Cox P. Wills D. Kiyashchenko-J. Lopez M. Costello S. Bourne G. Ugueto R. Lupton Mestayer, J. and G. Solano. Field trials of distributed acoustic sensing for geophysical monitoring. *SEG Technical Program Expanded Abstracts 2011*, pages 4253–4257, 2011.

[4] G. Jin and B. Roy. Hydraulic-fracture geometry characterization using low-frequency DAS signal. *Leading Edge*, 36(12):975–980, 2017.

[5] E. Holley and N. Kalia. Fiber-optic monitoring: Stimulation results from unconventional reservoirs. *Unconventional Resources Technology Conference, San Antonio, Texas, 20-22 July 2015*, Society of Exploration Geophysicists, American Association of Petroleum Geologists, Society of Petroleum Engineers, 2015.

[6] B. M. Freifeld J. Ajo-Franklin S. Dou R. Pevzner V. Shulakova S. Kashikar D. E. Miller J. Goetz J. Hennings et al. Daley, T. M. Field testing of fiber-optic distributed acoustic sensing (DAS) for subsurface seismic monitoring. *The Leading Edge*, 32(6):699–706, 2013.

[7] J. B. Ajo-Franklin, S. Dou, N. J. Lindsey, I. Monga, C. Tracy, M. Robertson, V. Rodriguez Tribaldos, C. Ulrich, B. Freifeld, T. Daley, and X. Li. Distributed Acoustic Sensing Using Dark Fiber for Near-Surface Characterization and Broadband Seismic Event Detection. *Scientific reports, nature.com*, 9(1):1328, 2019.

[8] Z. Li, Z. Shen, Y. Yang, E. Williams, X. Wang, and Z. Zhan. Rapid response to the 2019 Ridgecrest earthquake with distributed acoustic sensing. *AGU Advances*, 2(2):e2021AV000395, 2021.

[9] N. J. Lindsey, T. C. Dawe, and J. B. Ajo-Franklin. Illuminating seafloor faults and ocean dynamics with dark fiber distributed acoustic sensing. *Science*, 366:6469, 2019.

[10] M. Perton E. R. Martin-G. C. Beroza Spica, Z. J. and B. Biondi. Urban seismic site characterization by fiber-optic seismology. *Geophysical Research*, 125(3), 2020.

[11] A. Daneshy. Hydraulic fracturing of horizontal wells: Issues and insights. *in SPE Hydraulic Fracturing Technology Conference*, OnePetro, 2011.

[12] G. Jin K. Wu Liu, Y. and G. Moridis. Hydraulic-fracture-width inversion using Low-frequency distributed-acoustic-sensing strain data Part II: Extension for multifracture and field application. *SPE Journal*, 26(06):2703–2715, 2021a.

[13] G. Jin K. Wu Liu, Y. and G. Moridis. Hydraulic-fracture-width inversion using Low-frequency distributed-acoustic-sensing strain data Part I: Algorithm and sensitivity analysis. *SPE Journal*, 26 (01):359–371, 2021b.

[14] T. Parker C. Woerpel Y. Wu-R. Rufino Richter, P. and M. Farhadiroushan. Hydraulic fracture monitoring and optimization in unconventional completions using a high-resolution engineered fibre-optic Distributed Acoustic Sensor. *First Break*, 37(04):63–68, 2019.

[15] K. Suh S. Machovoe D. Byrd-M. Jaaskelainen H. Bland J. Stokes T. Henao N. Sahdev LeBlanc, M. Theory and Practice of a Flexible Fiber Optic Cable in a Horizontal Well Used for Cross Well and Microseismic Hydraulic Fracture Monitoring. *InSPE Hydraulic Fracturing Technology Conference and Exhibition*, 2022.

[16] K. T. Spikes, N. Tisato, T. E. Hess, and J. W. Holt. Comparison of geophone and surface-deployed distributed acoustic sensing seismic data. *Geophysics*, 84(2):A25–A29, 2019.

[17] S. Dou, N. Lindsey, A. M. Wagner, T. M. Daley, B. Freifeld, M. Robertson, J. Peterson, C. Ulrich, E. R. Martin, and J. B. Ajo-Franklin. Distributed Acoustic Sensing for Seismic Monitoring of The Near Surface: A Traffic-Noise Interferometry Case Study. *Scientific reports*, 7(1):11620, 2017.

[18] M. White, K. Friehauf, D. Cramer, J. Constantine, J. Zhang, S. Schmidt, J. Long, P. Mislan, J. Spenser, P. Meier, and E. Davis. One Stage Forward or Two Stages Back: What Are We Treating? Identification of Internal Casing Erosion during Hydraulic Fracturing—A Montney Case Study Using Ultrasonic and Fiber-Optic Diagnostics. *SPE Drilling Completion*, 36(02):383–397, 2021.

[19] D. D. Cramer and J. Zhang. Pressure-Based Diagnostics for Evaluating Treatment Confinement: SPE Production Operations. *SPE Production Operations*, 36:530–552, 2021.

[20] H. Schumann and G. Jin. Inferring hydraulic connectivity of induced fractures in the near-wellbore region using distributed acoustic sensing-recorded tube waves excited by perforation shots DAS tube-wave analysis. *Geophysics*, 87(3):D101–D109, 2022.

[21] M. Ehiwario A. Grae Ugueto, G. A. and M. Molenaar. Application of integrated advanced diagnostics and modeling to improve hydraulic fracture stimulation analysis and optimization. *SPE Hydraulic Fracturing Technology Converence*, OnePetro, 2014.

[22] K.T. Raterman, H.E. Farrell, O.S. Mora, A.L. Janssen, G.A. Gomez, S. Busetti, J. McEwen, K. Friehauf, J. Rutherford, R. Reid, and G. Jin. Sampling a stimulated rock volume: An eagle ford example. *SPE Reservoir Evaluation Engineering*, 21(04):927–941, 2018.

[23] G. Jin, K. Friehauf, B. Roy, J. J. Constantine, H. W. Swan, K. R. Krueger, and K. T. Raterman. Fiber optic sensing-based production logging methods for low-rate oil producers. *in SPE/AAPG/SEG Unconventional Resources Technology Conference: OnePetro*, 2019.

[24] S. Sakaida D. Zhu Pakhotina, I. and A. D. Hill. Diagnosing multistage fracture treatments with distributed fiber-optic sensors. *SPE Production Operations*, 35(04):852–864, 2020.

[25] R. S. Hurt Sookprasong, P. A. and C. C. Gill. Downhole monitoring of multicluster, multistage horizontal well fracturing with fiber optic distributed acoustic sensing (DAS) and distributed temperature sensing (DTS). *in International Petroleum Technology Conference*, OnePetro, 2014.

[26] P. Huckabee M. Wojtaszek T. Daredia Ugueto, G. and A. Reynolds. New near-wellbore insights from fiber optics and downhole pressure gauge data. *SPE hydraulic fracturing technology conference and exhibition*, OnePetro, 2019.

[27] S. A. Sonnenberg. Stratigraphic architecture of the Niobrara formation, Wattenberg field area, Colorado. *in Proceedings of the 4th Unconventional Resources Technology Conference, San Antonio, Texas, 1-3 August 2016*, Society of Exploration Geophysicists, American Association of Petroleum Geologists, Society of Petroleum Engineers, 2016.

[28] S. Sonnenberg. Geologic factors controlling production in the Codell sandstone, Wattenberg field, Colorado. *in Unconventional Resources Technology Conference, San Antonio, Texas, 20-22 July 2015*, Society of Exploration Geophysicists, American Association of Petroleum Geologists, Society of Petroleum Engineers, 2015.

[29] N. J. Lindsey, H. Rademacher, and J. B. Ajo-Franklin. On the broadband instrument response of fiber-optic DAS arrays. *Journal of Geophysical Research*, 125(2), 2020.

[30] E. Fidan Molenaar, M. M. and D. J. Hill. Real-time downhole monitoring of hydraulic fracturing treatments using fibre optic distributed temperature and acoustic sensing. *in SPE/EAGE European Unconventional Resources Conference and Exhibition*, OnePetro, 2012.

[31] D. Cramer, K. Friehauf, G. Roberts, and J. Whittaker. Integrating DAS, treatment pressure analysis and video-based perforation imaging to evaluate limited entry treatment effectiveness. *SPE Hydraulic Fracturing Technology Conference and Exhibition*, OnePetro, 2019.

[32] C.-H. Kuo, K.-L. Wen, H.-H. Hsieh, C.-M. Lin, T.-M. Chang, and K.-W. Kuo. Site classification and Vs30 estimation of free-field TSMIP stations using the logging data of EGDT. *Engineering Geology*, 2012.

[33] M. R. Najaftomarei, H. Rahimi, G. Tanircan, A. B. Mahani, and M. Shahvar. Site classification and probabilistic estimation of Vs30 for the Iranian strong-motion network. *Physics of the Earth and Planetary Interiors*, 308:106583, 2020.

[34] L. T. Brown, J. G. Diehl, R. L. Nigbor, and Others. A simplified procedure to measure average shear-wave velocity to a depth of 30 meters (VS30). volume proceedings of the 12th World Conference on Earthquake Engineering, Auckland, New Zealand, iitk.ac.in. Building Seismic Safety Council (BSSC), 2000.

[35] C. Comina, S. Foti, D. Boiero, and L. V. Socco. Reliability of VS30 evaluation from surface-wave tests. *Journal of Geotechnical and Geoenvironmental Engineering*, 137(6):579–586, 2011.

[36] A. Yong, E. M. Thompson, D. J. Wald, K. L. Knudsen, J. K. Odum, W. J. Stephenson, and S. Haefner. Compilation of VS30 data for the United States. *Data Series, US Geological Survey*, 2016.

[37] W. T. Dean and W.J. Seaton. Seismic Design Site Classification Using Spectral Analysis of Surface Waves (SASW) and Resistivity Imaging. *Site Characterization and Modeling*, pages 1–8, 2005.

[38] N. A. Abrahamson and W. J. Silva. Empirical Response Spectral Attenuation Relations for Shallow Crustal Earthquakes, journal=Seismological Research Letters. 68(1):94–127, 1997.

[39] M. Power, B. Chiou, N. Abrahamson, Y. Bozorgnia, T. Shantz, and C. Roblee. An Overview of the NGA Project. *Earthquake Spectra*, 24(1):3–21, 2008.

[40] D. M. Boore, E. M. Thompson, and H. Cadet. Regional correlations of VS30 and velocities averaged over depths less than and greater than 30 meters. *Bulletin of the Seismological Society of America, Seismological Society of America (SSA)*, 101(6):3046–3059, 2011.

[41] F. Garofalo, S. Foti, F. Hollender, P. Y. Bard, C. Cornou, B. R. Cox, M. Ohrnberger, D. Sicilia, M. Asten, G. Di Giulio, T. Forbriger, B. Guillier, K. Hayashi, A. Martin, S. Matsushima, D. Mercerat, V. Poggi, and H. Yamanaka. InterPACIFIC project: Comparison of invasive and non-invasive methods for seismic site characterization. Part I: Intra-comparison of surface wave methods. *Soil Dynamics and Earthquake Engineering*, 82:222–240, 2016.

[42] Kaoshan Dai and Xiaofeng Li. *Seismic Site Characterization through the Passive Surface Wave Survey.* Advances in Soil Dynamics and Foundation Engineering, American Society of Civil Engineers, 2014.

[43] S. Lin, N. Gucunski, S. Shams, and Y. Wang. Seismic site classification from surface wave data to VS30 without inversion. *Journal of Geotechnical and Geoenvironmental Engineering*, 147:04021029, 2021.

[44] J. Shragge, J. Yang, N. Issa, M. Roelens, M. Dentith, and S. Schediwy. Low-frequency ambient distributed acoustic sensing (DAS): case study from Perth, Australia. *Geophysical Journal International*, 226(1):564–581, 03 2021. ISSN 0956-540X. doi: 10.1093/gji/ggab111. URL https://doi.org/10.1093/gji/ggab111.

[45] K. E. Winters, M. C. Quinn, and Luis De Jesus-Diaz. Changes in Fiber-Optic Distributed Acoustic Sensing Noise Amplitude due to Tropical Depression Cristobal. *Geo-Extreme 2021, American Society of Civil Engineers*, pages 296–303, 2021.

[46] T. Zhu, J. Shen, and E. R. Martin. Sensing Earth and environment dynamics by telecommunication fiber-optic sensors: an urban experiment in Pennsylvania, USA. *Solid Earth*, 12(1):219–235, 2021.

[47] R. Krahenbuhl, B. Passerella, H. Flamme, G. Crookston, and D. Sirota. Developing a large underground geophysical education laboratory at Colorado School of Mines. *SEG Technical Program Expanded Abstracts 2018, Society of Exploration Geophysicists*, pages 2687–2691, 2018.

[48] C. B. Park, R. D. Miller, and J. Xia. Imaging dispersion curves of surface waves on multi-channel record. *SEG Technical Program Expanded Abstracts 1998, Society of Exploration Geophysicists*, pages 1377–1380, 1998.

[49] G. D. Bensen, M. H. Ritzwoller, M. P. Barmin, A. L. Levshin, F. Lin, M. P. Moschetti, N. M. Shapiro, and Y. Yang. Processing seismic ambient noise data to obtain reliable broad-band surface wave dispersion measurements. *Geophysical Journal International*, 169(3):1239–1260, 2007.

[50] G. Jin, J. B. Gaherty, G. A. Abers, Y. Kim, Z. Eilon, and W. R Buck. Crust and upper mantle structure associated with extension in the Woodlark Rift, Papua New Guinea from Rayleigh-wave tomography. *Geochemistry, Geophysics, Geosystems*, 16(11):3808–3824, 2015.

[51] I. G. Wong, K. H. Stokoe, B. R. Cox, Y.-C. Lin, and F.-Y. Menq. Shear-Wave Velocity Profiling of Strong Motion Sites that Recorded the 2001 Nisqually, Washington, Earthquake. *Earthquake Spectra*, 27(1):183–212, 2011.

[52] N. H. Harinarayan and Abhishek Kumar. Site Classification of the Strong Motion Stations of Uttarakhand, India, Based on the Model Horizontal to Vertical Spectral Ratio. *Geotechnical Frontiers 2017*, pages 141–149, 2017.

APPENDIX A

CHAPTER 1 SUPPLEMENTAL INFORMATION

A.1 Perforation and Plug Depth Location

Determination of the perforation and bridge plug depth locations is critical for diagnosing stage isolation and the degree of inter-stage fluid communication. Depth information provided by Great Western Petroleum is used as a first-degree initial estimate. We plot the in-well DAS data for the four targeted stages (Figure A.1 top), including the temporal acoustic energy summation (Figure A.1 bottom), using the 500-5000 Hz frequency band which was preprocessed by the service provider. The y-axis indicates time (ascending top to bottom) and the x-axis indicates the measured depth along the wellbore (heel to toe). The dashed black lines represent the estimated perforation locations. Assuming a correlation between acoustic intensity and fluid flow, events recorded by in-well DAS can be used to align the measured depths between perforations and DAS channels.

Qualitative observations provide an approximate location; however, it is difficult to distinguish individual perforations. We applied several bandpass filters to better identify assumed perforation noise, but the differences were negligible for determining individual perforations. The temporal energy summation (Figure A.1 bottom) provides the energy profile along the stage intervals, where the peak amplitudes are assumed to align with perforation locations. We used the high amplitude peaks recorded at the toe-side clusters as our proxy and apply a 10 ft bulk shift to the perforation depth locations. We make this interpretation based on the following:

- Not all perforations align with a peak amplitude in the summation plots (Figure A.1 bottom). Specifically, for 12 perforations, we would ideally observe twelve well defined amplitude peaks separated by troughs. This absence is possibly due to uneven fluid distribution across the perforations, and/or near-well bore region effects (i.e., fractures along the wellbore).

- The perforation(s) at the toe-side of the targeted stage interval record the highest acoustic intensity. This is likely due to positional bias, with toe-side clusters receiving a greater amount of proppant. Deneshy [11] observed separation between proppant and fluid, with an excess of proppant traveling to the toe-side clusters due to inertia.

We also compute the RMS amplitude (see section 2.4) to support our interpretations. Figure A.2 shows the RMS amplitudes, plotted against depth, for each treatment stage. The black dots indicate the perforation locations and are shifted along the y-axis to visually differentiate between stages. Applying the

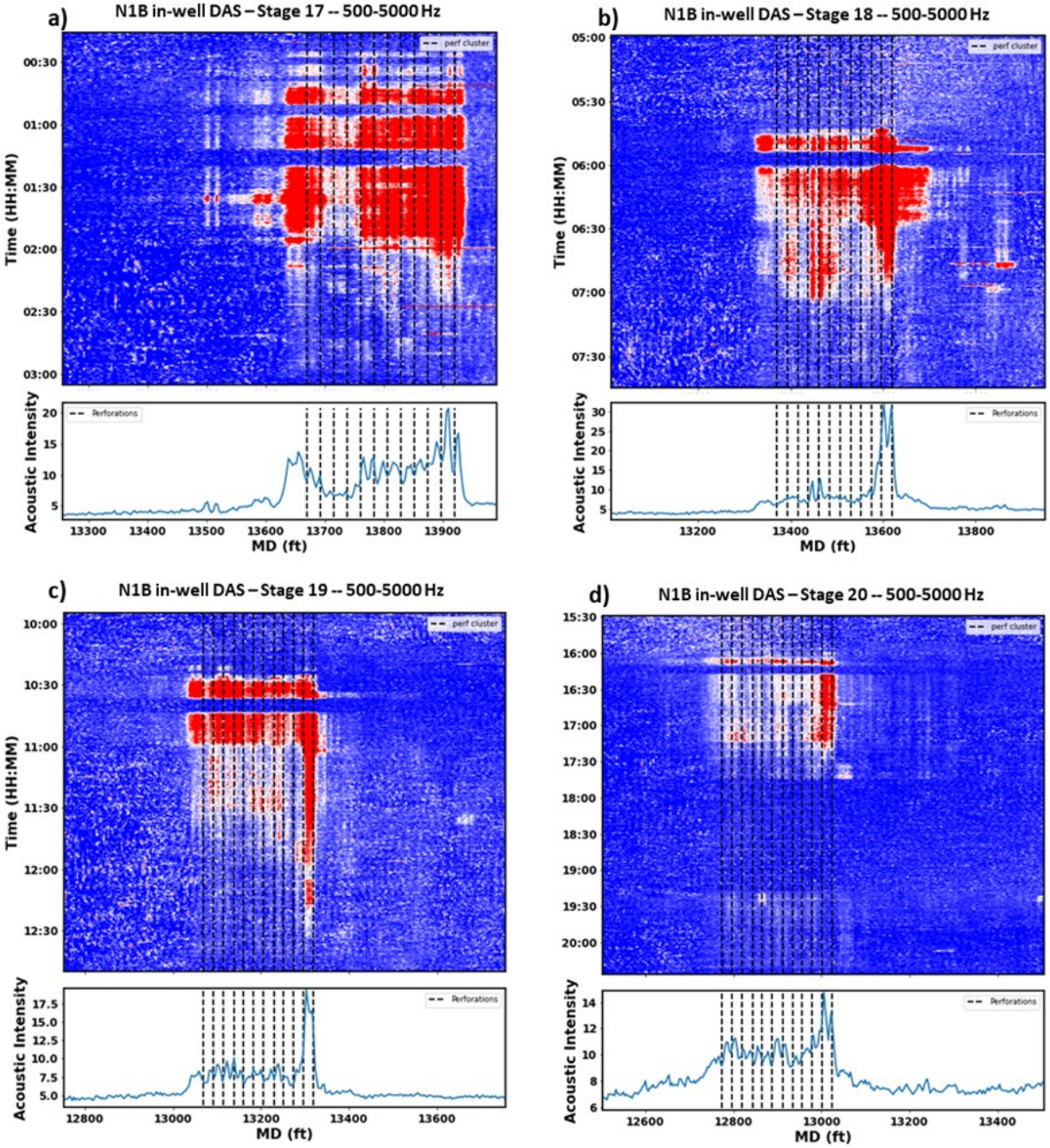

Figure A.1 In-well DAS (top) recorded in well N1B processed at 500-5000 Hz with temporal acoustic intensity summation (bottom) including (a) stage 17, (b) stage 18, (c) stage 19, and (d) stage 20. The black dashed lines mark the estimated perforation locations.

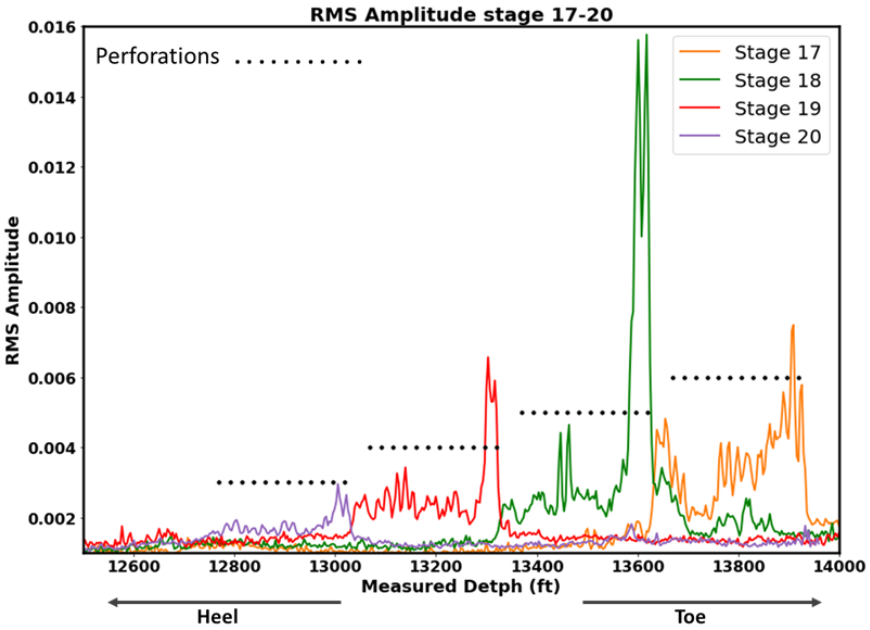

Figure A.2 RMS amplitude calculated from in-well DAS (500 - 5000 Hz) for stages 17-20. The black dots indicate the perforation measured depth locations. Offset in the y-direction is to differentiate stages.

10 ft bulk shift in depth aligns the perforations with the high amplitude toe-side signals and confines them within the stage intervals.

A.2 In-well DAS Acoustic Intensity Attribute

The static in-well DAS attribute (see section 2.4) serves as a semi-quantitative method to characterize the total acoustic intensity recorded within the targeted, and adjacent treatment stages. Figure A.3 shows the acoustic intensity recorded during treatment stage 20 as an example. The dashed black lines indicate the bridge plug depths, and the red dashed lines indicate the depth interval used to calculate the "noise-floor". The process is as follows:

- Window data spatially according to plug set depth (i.e. between the black dashed lines).
- Window data temporally according to the start and end time of the treatment.
- Compute the absolute sum (i.e., sum across the spatial and temporal axis of the data).
- Repeat the process to compute the noise-floor for each treatment stage using an upstream depth interval with relatively little noise.

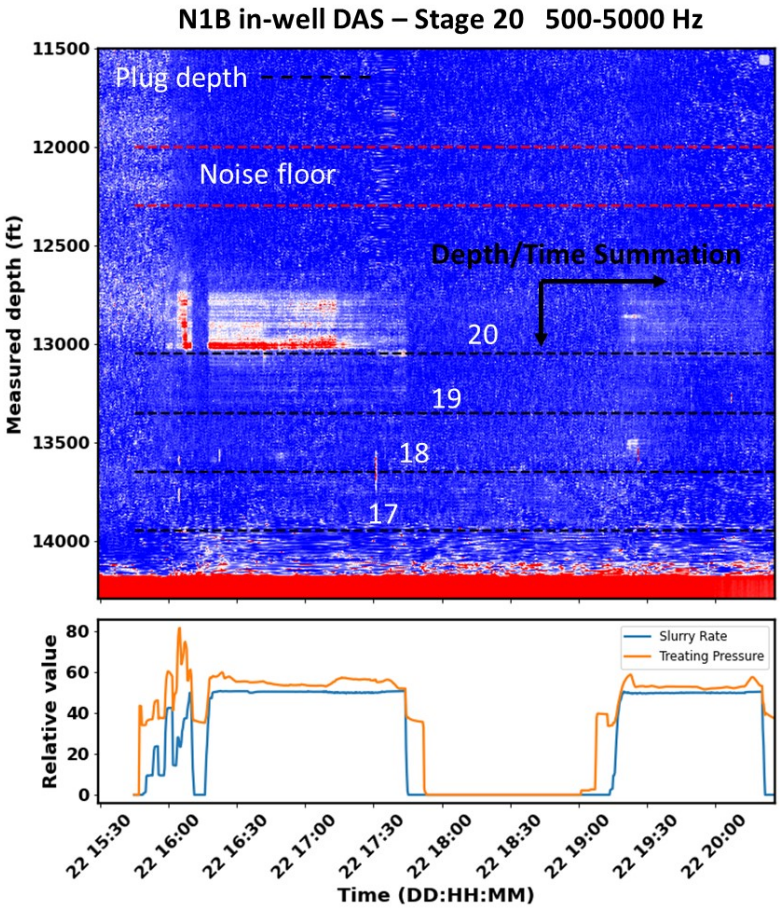

Figure A.3 In-well DAS recorded during treatment stage 20 (top) and associated pumping curve (bottom). The dashed black lines indicate the bridge plug measured depth for each stage. The red dashed line indicates the interval selected to calculate the noise-floor.

A.3 LF-DAS pre-inversion Processing

It is necessary to preprocess the LF-DAS data prior to inversion to avoid unreliable fracture width results. Note that preprocessing steps may vary based on the quality of data (i.e., background noise, temporal resolution, interrogator used for acquisition). The challenge is to filter the data while minimally impacting the targeted extension and compression signal(s) induced by fracture hits. The first step in our process is defining a data window upstream from the targeted treatment interval. The upstream interval is preferred because we assume the formation has not been affected from any downstream treatment stages in the injection well. The median is calculated along the temporal axis for each DAS channel in the selected window and subtracted from the entire LF-DAS dataset to remove the low-frequency background drift noise that is most likely associate with interrogator noise [4]. We then apply a median filter (3x5 kernel) on the entire dataset to remove the "spikey noise" (Figure A.4) which is commonly observed in LF-DAS data (e.g., [4][14]). We postulate this noise is due to mechanical decoupling as the formation extends and compresses spatially along the fiber.

To aid in the fracture picking process, we extend the LF-DAS data by a sufficient amount of time prior to injection and after injection ends. In Figure A.4 we observe previous stage fractures closing prior to injection. After injection ends, we observe a polarization in the strain signal which is a key indicator of the fracture(s) measured depth location.

A.4 Field Strain vs Model Prediction

Figure A.5 show the LF-DAS waterfall plots including the field strain change used for inversion (Figure A.5a and Figure A.5d) and the predicted model strain using the inverted widths (Figure A.5b and Figure A.5e) for stages 17 and 18. The field strain and model predicted strain match well suggesting confidence in our inversion results. For a more straightforward comparison, Figure A.5c and Figure A.5f show the field strain and model predicted strain for a specific timestep near the end of the treatment for stage 17 and 18, respectively. Figure A.6 shows the same results for stages 19 and 20. In general, all stages show good agreement between the field and predicted strain.

The extension strain data at the fracture hit location is removed prior to inversion. LF-DAS data may not accurately represent fracture-induced strain at the fracture hit location due to mechanical decoupling and thermal effects [12]. When the fracture approaches the fiber, the separation between the cement/formation and the fiber may cause measurement bias, impacting the accuracy of the inversion results. Thermal effects may also result from direct hydraulic fracturing fluid contact with the fiber, introducing additional bias.

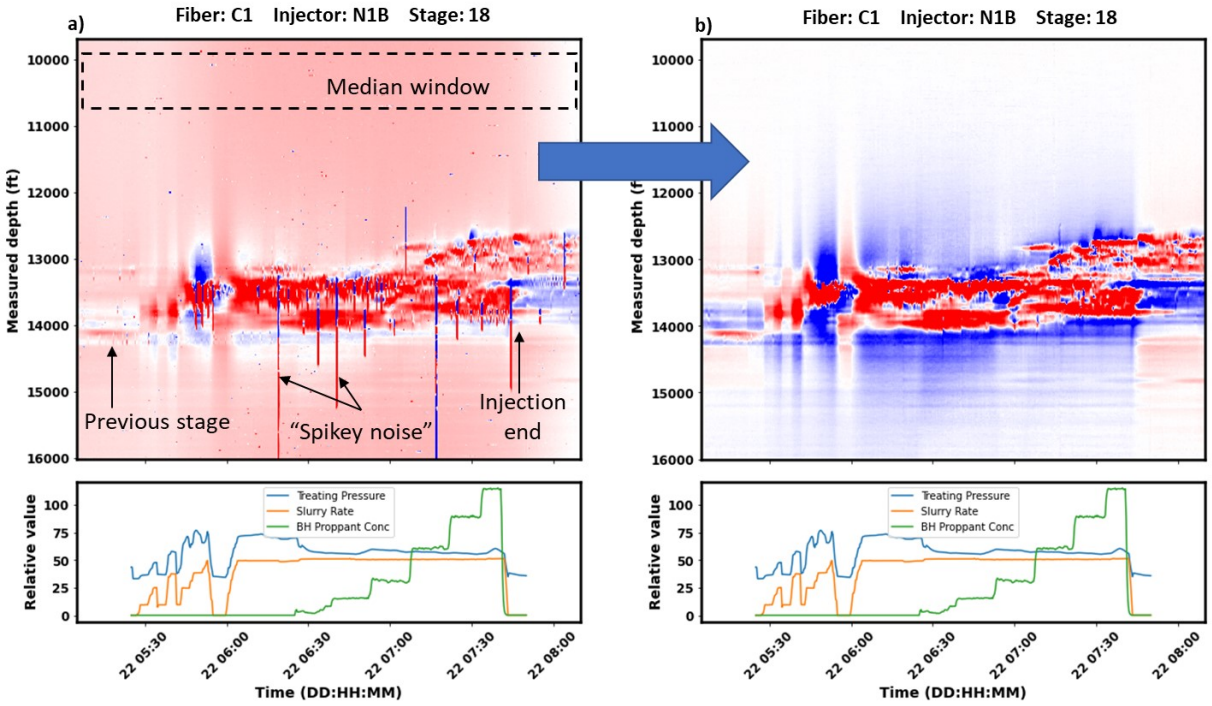

Figure A.4 LF-DAS data for treatment stage 18 (top) and associated pumping curves (bottom). (a) Pre-processed LF-DAS data and (b) post processing LF-DAS data.

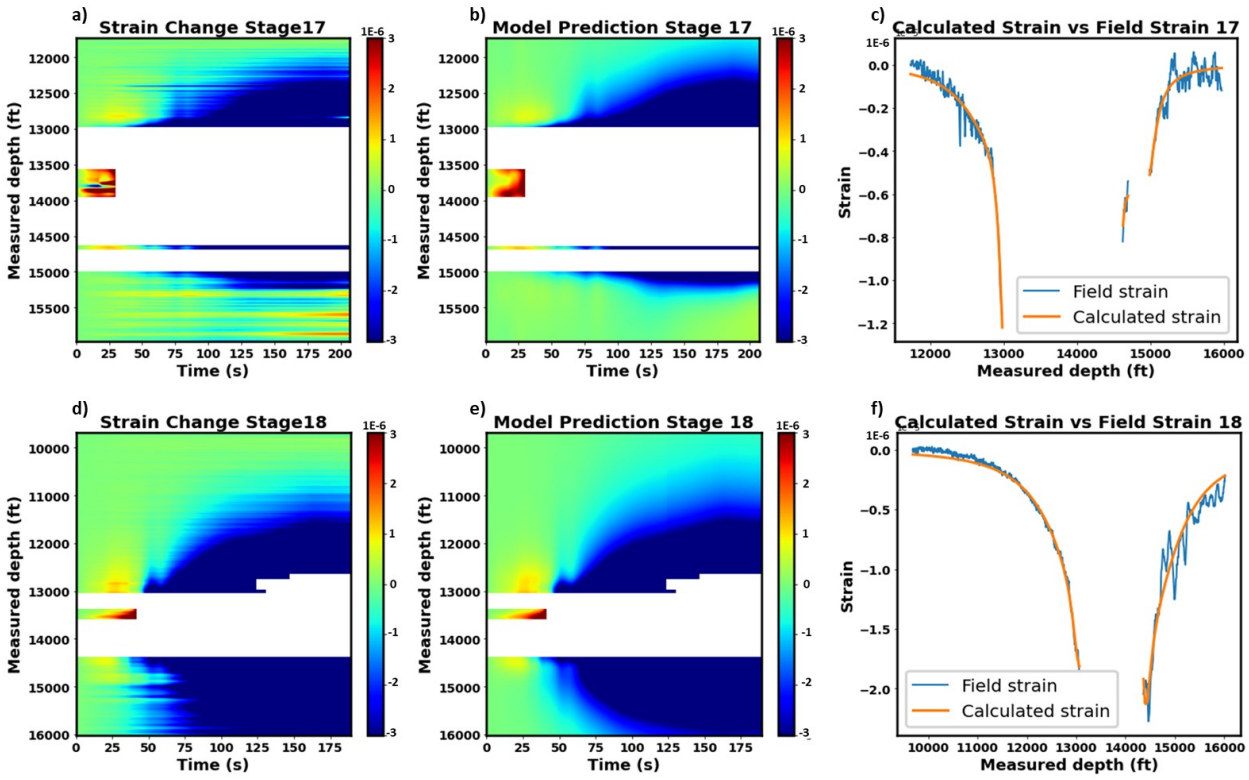

Figure A.5 LF-DAS waterfall plots representing the field strain (a and d) and model predicted strain (b and e) for stage 17 and 18. (c) and (f) compare the predicted strain and field strain at a specific time step.

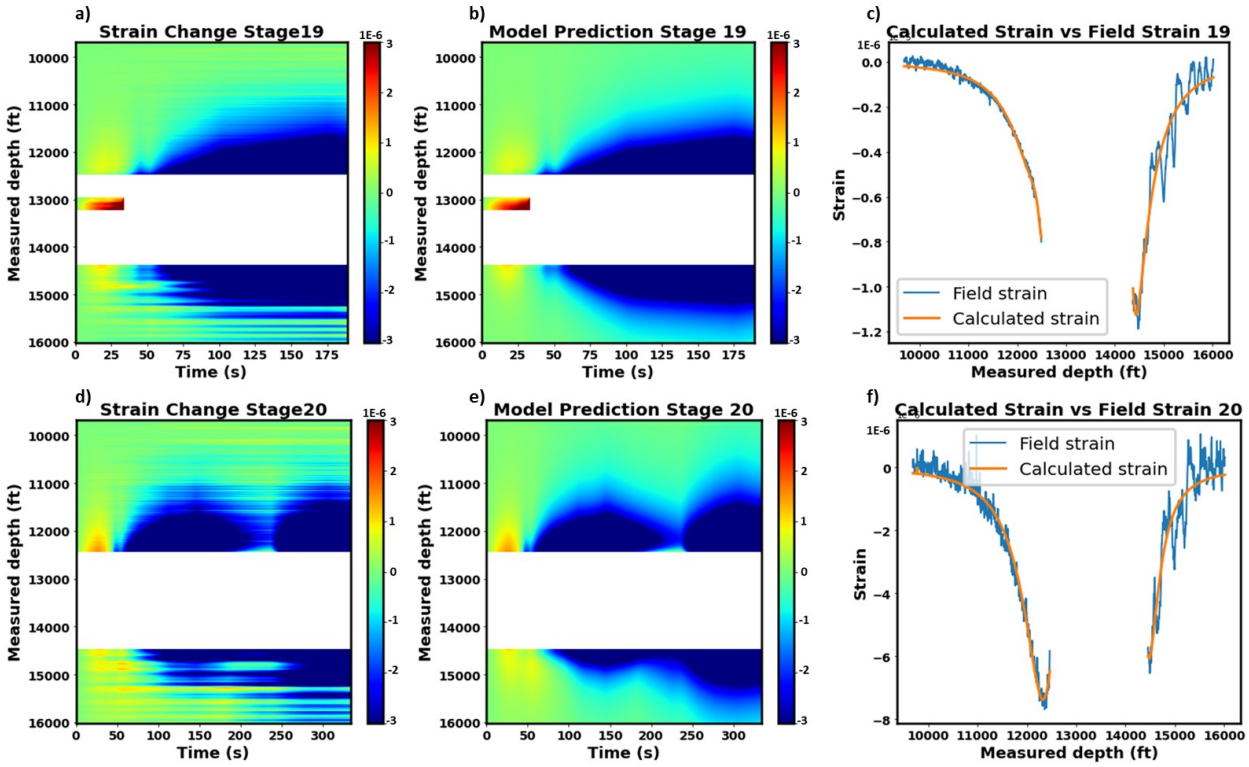

Figure A.6 LF-DAS waterfall plots representing the field strain (a and d) and model predicted strain (b and e) for stage 17 and 18. (c) and (f) compare the predicted strain and field strain at a specific time step.

APPENDIX B

CHAPTER 2 SUPPLEMENTAL INFORMATION

B.1 Spatial Coupling Variation Example

Ambient waveform static results (Figure 3.2) provide qualitative insights regarding the coupling condition at one virtual source (DAS channel) for each subsection. However, the interformetric process (see section 3.3) results in a 3D volume of waveforms, where each DAS channel acts as a virtual source and receiver. Scanning through each DAS channel provides a quick, qualitative analysis of how the coupling condition varies across the entire field for each subsection.

The Snow Pressed and Snow subsections provide an intuitive example of how coupling conditions can effect the quality of the recorded signal. Figure B.1 is a map view of Kafadar Field, indicating the approximate location and direction of DAS channels (in ascending order).

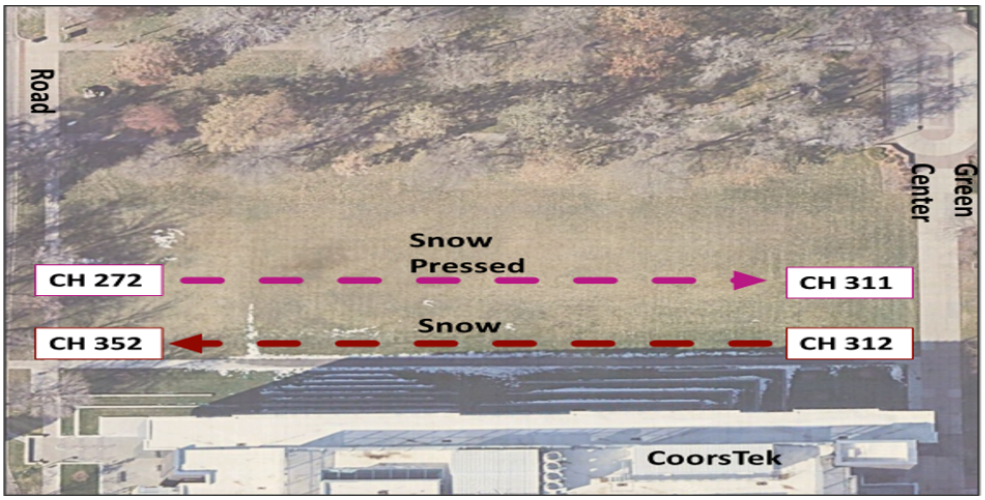

Figure B.1 Map view of Kafadar Field. The purple and red lines indicate the location and ascending channel direction of the Snow Pressed and Snow subsections, respectfully.

Figure B.2 shows the ambient waveforms recorded along the Snow Pressed subsections at four different DAS channels. In general, we observe a strong signal response indicated by high amplitude waveforms and moveouts for each of the DAS channels. Coherent signals are strongest closer to the road, and begin to diminish as the virtual source moves toward the Green Center.

In contrast, Figure B.3 shows that the Snow subsection records very little coherent waveforms for most of the virtual sources. This indicates insufficient coupling with the Snow for DAS to record any notable surface wave signals. However, as the virtual source becomes closer to the road, we observe some coherency

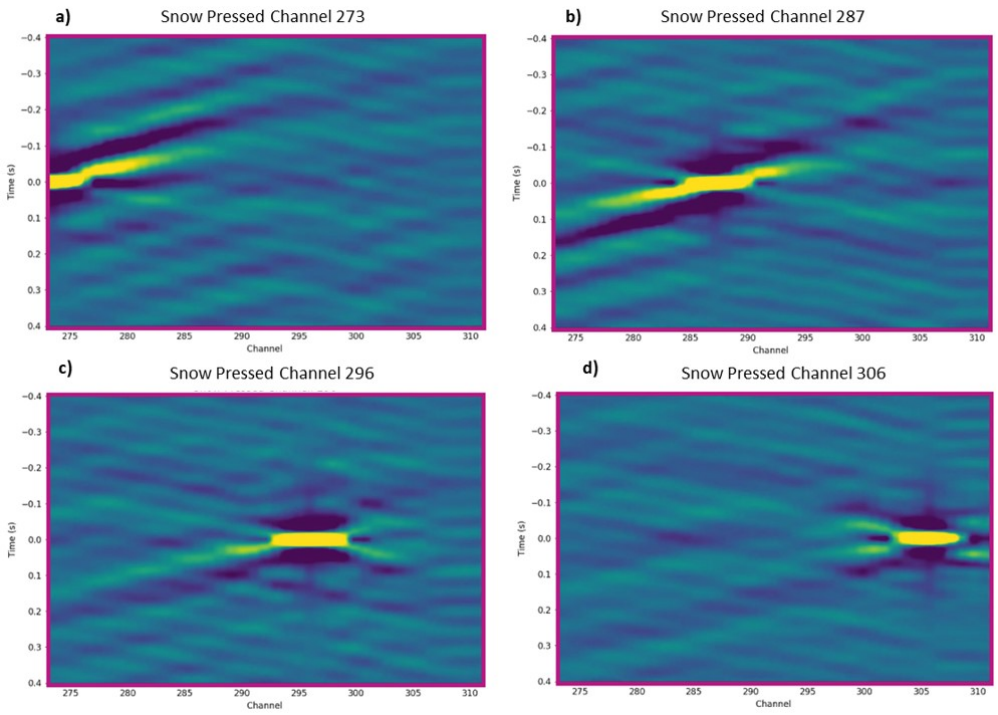

Figure B.2 Ambient waveforms recorded along Snow Pressed subsection showing how coupling varies spatially across Kafadar Field. From west to east: (a) channel 273, (b) channel 287, (c) channel 296, and (d) channel 306.

and moveout in the waveforms. Assuming continuous coupling along the Snow subsection, this demonstrates the sensitivity of DAS to record surface waves despite relatively poor coupling.

Several important conclusions can be made from this example alone:

- Light coupling (i.e. pressing fiber into the ground) can provide enough fiber-ground contact to leverage the high sensitivity of DAS to record surface waves.
- Surface deployments with DAS require careful consideration of array orientation and proximity to ambient sources in the survey area. The process presented in this study may overcome the challenges of unfavorable coupling by simply deploying fiber closer to dominant energy sources.
- Despite the challenge of incoherent signal for most of the Snow subsection, the process presented in this study produced consistent VS30 results compared with the other subsections. This suggests that as little as a few tens of meters of sufficient coupling can be used for near-surface surveys (i.e. VS30 assessments).
- Our methodology can be modified and automated to make quick in-the-field assessments. This allows technicians to quickly scan the data (i.e. scan through virtual sources) and determine if array

reconfiguration is necessary to improve recorded signal quality.

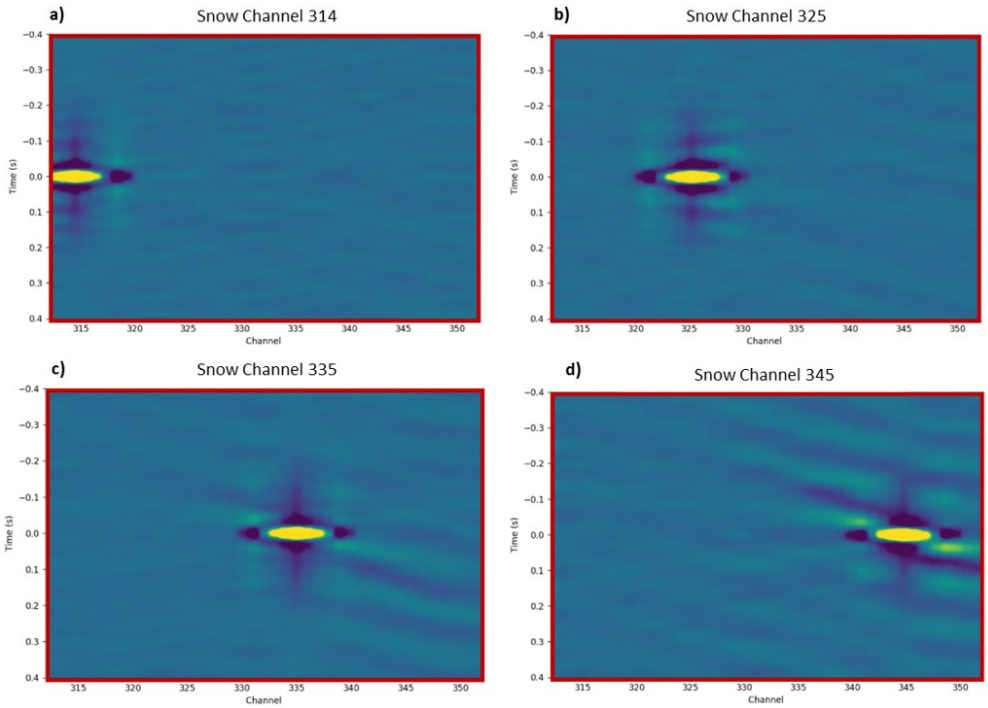

Figure B.3 Ambient waveforms recorded along Snow subsection showing how coupling varies spatially across Kafadar Field. From east to west: (a) channel 334, (b) channel 325, (c) channel 335, and (d) channel 345.